Petroleum Science 23 (2026) 4686–4703

Contents lists available at ScienceDirect

Petroleum Science

journal homepage: www.keaipublishing.com/en/journals/petroleum-science

Original Paper

Influence mechanism of adjacent formation interfaces on acoustic wave modes in horizontal wells

Zhi-Yang Lei [a,b], Yi Xin [c], Dong Wu [d], Ming Cai [a,b,*], Xin-Jian Zhao [c], Cheng-Guang Zhang [a,b], Yuan-Jun Zhang [a,b], Shi-Hong Luo [a,b]

[a] Key Laboratory of Oil and Gas Resources and Exploration Technology of Ministry of Education, Yangtze University, Wuhan, 430100, Hubei, China
[b] School of Geophysics and Petroleum Resources, Yangtze University, Wuhan, 430100, Hubei, China
[c] Tarim Oilfield Company, PetroChina, Korla, 841000, Xinjiang, China
[d] Information Center, CNPC Engineering Technology Research Institute, Beijing, 102206, China

ARTICLE INFO

Article history:
Received 13 October 2025
Received in revised form
26 December 2025
Accepted 15 April 2026
Available online 22 April 2026

Edited by Meng-Jiao Zhou

Keywords:
Acoustic logging
Formation interfaces
Horizontal wells
Numerical simulation
Borehole wave modes

ABSTRACT

Although horizontal well technology has been widely adopted in hydrocarbon exploration, acoustic logging interpretation remains challenging under complex formation conditions, particularly when formation interfaces are located adjacent to the borehole. This study systematically investigates acoustic wave propagation in horizontal boreholes through numerical modeling, focusing on formation interface effects. Numerical models with varying positions and numbers of interfaces were developed, and 3D finite-difference wavefield simulations were performed. Wave mode characteristic parameters (velocity, energy, and dominant frequency) of full-wave array data from these models were extracted to analyze the effects of formation interfaces. Results demonstrate that P-waves are more sensitive to formation interfaces than S-waves, exhibiting distinct variations in propagation velocity, energy enhancement, and frequency fluctuation. In contrast, S-waves maintain stable propagation velocities with only minor perturbations in energy and frequency. Wavefield snapshots clearly show that P-waves in the faster outer formation gradually overtake those in the slower inner formation, arriving earlier at receivers. Furthermore, closer interfaces induce earlier wave overlap, while increasing interface distance delays the overtaking of the slow P-wave by the fast P-wave, and sufficiently distant interfaces completely prevent the overtaking. The proposed theory remains valid for complex formations involving multiple coupled interfaces and small-dip tilted interfaces. These findings elucidate the underlying mechanism of formation interface effects on acoustic wave modes within horizontal wells, providing a theoretical basis for accurate parameter extraction and correction.

1. Introduction

Horizontal wells typically achieve several times the production rates of conventional vertical wells, thereby significantly enhancing single-well production and oil and gas recovery (Feng, 2023; Su, 2018). As a result, they play a critical role in the exploration and development of oil and gas fields. However, interpretation methods for acoustic logging data in horizontal wells remain challenging, as the recorded waveforms are often influenced by multiple complex factors. Consequently, conventional interpretation methods developed for vertical wells cannot be directly applied to horizontal wells without adjustment (Liu, 2021; Passey et al., 2005; Zhou and Wang, 2006). For acoustic logging, a key influencing factor is the presence of adjacent high-velocity formation, which can markedly affect the propagation and attenuation behavior of borehole wave modes (Huang and Torres-Verdín, 2017; Wang et al., 2017). Therefore, clarifying this influence mechanism is essential for improving the accuracy and reliability of acoustic logging interpretation in horizontal wells.

During the acoustic logging process, elastic waves are excited by a transmitter and propagate through the formation, carrying formation information to the receiver. Thus, characteristics such as velocity, amplitude (or energy) and frequency of the borehole

* Corresponding author.
E-mail address: caiming@yangtzeu.edu.cn (M. Cai).
Peer review under the responsibility of China University of Petroleum (Beijing).

https://doi.org/10.1016/j.petsci.2026.04.027
1995-8226/

wave modes can reflect formation properties, including those of the reservoir (Wang et al., 2020). Currently, the velocities of P-waves and S-waves in full-waveform acoustic logging are routinely employed to calculate the elastic and anelastic parameters of the formation, estimate formation pressure, compute porosity, and assess the reservoir (Qiao et al., 2011). The velocities and amplitude attenuation of S-waves and Stoneley waves are highly sensitive to fractures, making them particularly effective for fracture and vuggy detection, as well as reservoir permeability inversion (Cai et al., 2020, 2022b; Rostami et al., 2022; Yang et al., 2019), even acoustic noise signals can be monitored to locate casing leaks in wells (Li et al., 2022). Therefore, accurately extracting wave mode characteristic parameters is essential for precise reservoir evaluation. Meanwhile, as exploration and development increasingly target complex reservoirs, acoustic logging technology has continued to advance to provide richer formation information and support more accurate, multi-scale reservoir evaluation. Tool designs have evolved from early monopole sources to dipole, multipole and phased-array configurations, thereby expanding the range of borehole wave modes that can be effectively excited and recorded. These developments have also facilitated the emergence of advanced acoustic techniques—such as logging-while-drilling acoustics, borehole acoustic reflection imaging—which have been developed and refined based on the operating principles and functional characteristics of different acoustic tool designs (Che et al., 2009; Ma et al., 2025; Qiao et al., 2011; Wood, 2024).

Building on these acoustic logging methods, numerous researchers worldwide have conducted extensive studies on the accurate extraction and correction of borehole wave mode parameters. In the domain of acoustic slowness logging, researchers found that the dip angle in transversely isotropic (TI) formations affects the acoustic slowness in wells. Through simulation and analysis of wavefields with different sources, the derived correction charts are effective in calibrating acoustic slowness in deviated wells (Lin et al., 2006; Randall et al., 1991; Wei and Chen, 2015). In addition, fast formations could influence the acoustic slowness of wave modes in horizontal wells (Liu et al., 2017). When the borehole axis coincides with the formation interface, the P-wave slowness in the borehole approaches that of the fast formation (Cong and Qiao, 2008). However, the underlying patterns and mechanisms remain insufficiently explained.

Significant efforts have been made to investigate factors influencing the amplitude and energy of wave modes. Through extensive numerical simulations and physical experiments, researchers have identified fracture width, dip angle, fracture-filling fluid, and cavity shape as the primary factors affecting wave mode amplitudes (Cai et al., 2020, 2022b; Gao et al., 2024; Liu et al., 2025; Xu and Wang, 2020). Wave mode conversions at fractures induce amplitude attenuation of borehole wave modes (Pan et al., 2022). These attenuation patterns are inversely utilized for fracture and cavity evaluation, leading to the development of intelligent evaluation schemes and geological reflection interface azimuth inversion methods (Cai et al., 2022a; Pan et al., 2023).

Researchers have revealed additional factors that affect borehole wave modes, such as formation interface reflections (Hei et al., 2024), formation anisotropy (Wang et al., 2017), tool eccentricity (Wang and Qiao, 2014; Zhang et al., 2024), and borehole enlargement (Su et al., 2022). These findings have facilitated the development of a novel 3D acoustic logging tool (Liu et al., 2016), an advanced azimuthal phased-array acoustic logging method (Wang et al., 2017), and improved techniques for compensating tool eccentricity effects (Ji et al., 2021). However, existing research has primarily focused on the impact patterns of an adjacent fast formation on P-wave slowness, while paying limited attention to the responses of other wave modes and the underlying mechanisms (Liu et al., 2017).

The main differences between this study and previous work are as follows: First, we systematically investigated the effects of formation interfaces on the velocity, energy, and dominant frequency of borehole wave modes. This study also revealed a novel P-wave energy attenuation pattern, which could be applied to develop a method for locating formation interfaces. Second, we clarified the underlying mechanisms of formation interface effects on horizontal borehole wave modes, and subsequently applied these findings to extended low-dip interface and multi-interface formation models. The structure of this paper is as follows: First, the numerical simulation method for array acoustic logging is introduced, and models with different formation interface positions are constructed. Then, the effects of formation interfaces on wave mode characteristic parameters at various transmitter-receiver spacings are analyzed. Thereafter, wavefield snapshots are utilized to investigate the underlying mechanisms governing wave mode responses. Subsequently, we extended the investigation to low-dip interface and multi-interface formation models, to obtain the wave mode response pattern under inclined and multiple interface conditions. Finally, the main conclusions of this study are systematically summarized.

2. Numerical simulation of array acoustic logging based on the finite-difference (FD) method

Alford et al. (1974) first applied the Finite-Difference (FD) to simulate acoustic wave propagation in elastic media. Later, Stephen et al. (1985) employed this method to simulate the acoustic field in fluid-filled boreholes, demonstrating the feasibility of the FD method for numerical acoustic logging simulations. These pioneering works laid the foundation for the widespread application of FD techniques in modern elastic wave simulation and acoustic logging analysis (Chen et al., 2006; Ma et al., 2019; Wang et al., 2003; Yang et al., 2018; Zhao et al., 2007).

2.1. Implementation of the FD algorithm for acoustic logging

This study employs the 3D Staggered-Grid Finite-Difference (SGFD) method to simulate acoustic wavefields (Graves, 1996). Based on elastic theory and under the assumption of no external forces, the first-order velocity-stress elastic wave equations in Cartesian coordinate system are derived as in Eq. (1).

$$\begin{cases} \dfrac{\partial \tau_{xy}}{\partial t} = \mu\left(\dfrac{\partial v_x}{\partial y} + \dfrac{\partial v_y}{\partial x}\right), \rho\dfrac{\partial v_x}{\partial t} = \dfrac{\partial \tau_{xx}}{\partial x} + \dfrac{\partial \tau_{xy}}{\partial y} + \dfrac{\partial \tau_{xz}}{\partial z} \\ \dfrac{\partial \tau_{yz}}{\partial t} = \mu\left(\dfrac{\partial v_y}{\partial z} + \dfrac{\partial v_z}{\partial y}\right), \rho\dfrac{\partial v_y}{\partial t} = \dfrac{\partial \tau_{yx}}{\partial x} + \dfrac{\partial \tau_{yy}}{\partial y} + \dfrac{\partial \tau_{yz}}{\partial z} \\ \dfrac{\partial \tau_{xz}}{\partial t} = \mu\left(\dfrac{\partial v_x}{\partial z} + \dfrac{\partial v_z}{\partial x}\right), \rho\dfrac{\partial v_z}{\partial t} = \dfrac{\partial \tau_{zx}}{\partial x} + \dfrac{\partial \tau_{zy}}{\partial y} + \dfrac{\partial \tau_{zz}}{\partial z} \\ \dfrac{\partial \tau_{xx}}{\partial t} = \lambda\left(\dfrac{\partial v_y}{\partial y} + \dfrac{\partial v_z}{\partial z}\right) + (\lambda + 2\mu)\dfrac{\partial v_x}{\partial x} \\ \dfrac{\partial \tau_{yy}}{\partial t} = \lambda\left(\dfrac{\partial v_x}{\partial x} + \dfrac{\partial v_z}{\partial z}\right) + (\lambda + 2\mu)\dfrac{\partial v_y}{\partial y} \\ \dfrac{\partial \tau_{zz}}{\partial t} = \lambda\left(\dfrac{\partial v_x}{\partial x} + \dfrac{\partial v_y}{\partial y}\right) + (\lambda + 2\mu)\dfrac{\partial v_z}{\partial z} \end{cases} \quad (1)$$

In the equation, x, y, and z are the spatial coordinates; t is the time; ρ is the density; λ and μ are the Lamé coefficients; τ_{ii} represents the normal stresses, and τ_{ij} represents the shear stresses; v_x, v_y, and v_z are the velocity components.

The foregoing equations are discretized using an SGFD scheme (Chen et al., 2006). The spatial locations of different physical components within a computational octant are shown in Fig. 1. The sampling locations for elastic parameters coincide with those of normal stress, and the sampling times are staggered between velocity and stress components.

Using Taylor expansion, the $2N$-order SGFD operator can be derived as follows:

$$\delta_{2N} f = \frac{1}{\Delta x} \sum_{m=0}^{N-1} a_m \left[f\left(x + \frac{2m+1}{2}\Delta x\right) - f\left(x - \frac{2m+1}{2}\Delta x\right) \right] \tag{2}$$

In the equation, $\delta_{2N} f$ is the $2N$-order SGFD operator, where a_m represents the SGFD approximation coefficients. Some of these coefficients are listed in Table 1.

By discretizing Eq. (1) using the difference operator in Eq. (2), the corresponding difference equation is given by:

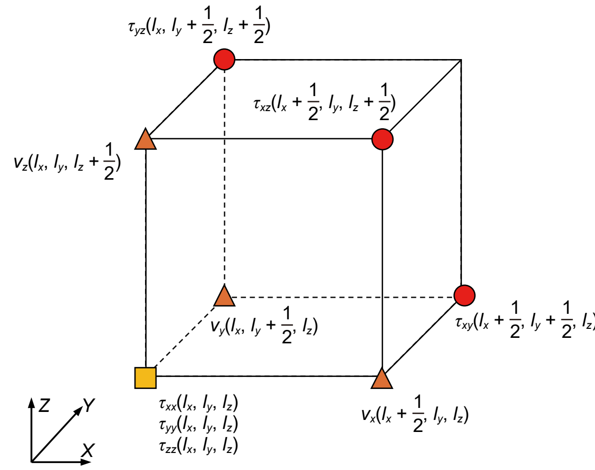

Fig. 1. Spatial locations of physical parameters in the staggered-grid scheme.

$$\begin{cases}
\rho_{l_x+\frac{1}{2},l_y,l_z} \delta_t (v_x)^n_{l_x+\frac{1}{2},l_y,l_z} = \delta_x(\tau_{xx})^n_{l_x+\frac{1}{2},l_y,l_z} + \delta_y(\tau_{xy})^n_{l_x+\frac{1}{2},l_y,l_z} + \delta_z(\tau_{xz})^n_{l_x+\frac{1}{2},l_y,l_z} \\
\rho_{l_x,l_y+\frac{1}{2},l_z} \delta_t (v_y)^n_{l_x,l_y+\frac{1}{2},l_z} = \delta_x(\tau_{yx})^n_{l_x,l_y+\frac{1}{2},l_z} + \delta_y(\tau_{yy})^n_{l_x,l_y+\frac{1}{2},l_z} + \delta_z(\tau_{yz})^n_{l_x,l_y+\frac{1}{2},l_z} \\
\rho_{l_x,l_y,l_z+\frac{1}{2}} \delta_t (v_z)^n_{l_x,l_y,l_z+\frac{1}{2}} = \delta_x(\tau_{zx})^n_{l_x,l_y,l_z+\frac{1}{2}} + \delta_y(\tau_{zy})^n_{l_x,l_y,l_z+\frac{1}{2}} + \delta_z(\tau_{zz})^n_{l_x,l_y,l_z+\frac{1}{2}} \\
\delta_t(\tau_{xx})^{n+\frac{1}{2}}_{l_x,l_y,l_z} = (\lambda+2\mu)_{l_x,l_y,l_z} \delta_x(v_x)^{n+\frac{1}{2}}_{l_x,l_y,l_z} + \lambda_{l_x,l_y,l_z} \delta_y(v_y)^{n+\frac{1}{2}}_{l_x,l_y,l_z} + \lambda_{l_x,l_y,l_z} \delta_z(v_z)^{n+\frac{1}{2}}_{l_x,l_y,l_z} \\
\delta_t(\tau_{yy})^{n+\frac{1}{2}}_{l_x,l_y,l_z} = \lambda_{l_x,l_y,l_z} \delta_x(v_x)^{n+\frac{1}{2}}_{l_x,l_y,l_z} + (\lambda+2\mu)_{l_x,l_y,l_z} \delta_y(v_y)^{n+\frac{1}{2}}_{l_x,l_y,l_z} + \lambda_{l_x,l_y,l_z} \delta_z(v_z)^{n+\frac{1}{2}}_{l_x,l_y,l_z} \\
\delta_t(\tau_{zz})^{n+\frac{1}{2}}_{l_x,l_y,l_z} = \lambda_{l_x,l_y,l_z} \delta_x(v_x)^{n+\frac{1}{2}}_{l_x,l_y,l_z} + \lambda_{l_x,l_y,l_z} \delta_y(v_y)^{n+\frac{1}{2}}_{l_x,l_y,l_z} + (\lambda+2\mu)_{l_x,l_y,l_z} \delta_z(v_z)^{n+\frac{1}{2}}_{l_x,l_y,l_z} \\
\delta_t(\tau_{xy})^{n+\frac{1}{2}}_{l_x+\frac{1}{2},l_y+\frac{1}{2},l_z} = \mu_{l_x+\frac{1}{2},l_y+\frac{1}{2},l_z} \left[\delta_y(v_x)^{n+\frac{1}{2}}_{l_x+\frac{1}{2},l_y+\frac{1}{2},l_z} + \delta_x(v_y)^{n+\frac{1}{2}}_{l_x+\frac{1}{2},l_y+\frac{1}{2},l_z} \right] \\
\delta_t(\tau_{xz})^{n+\frac{1}{2}}_{l_x+\frac{1}{2},l_y,l_z+\frac{1}{2}} = \mu_{l_x+\frac{1}{2},l_y,l_z+\frac{1}{2}} \left[\delta_z(v_x)^{n+\frac{1}{2}}_{l_x+\frac{1}{2},l_y,l_z+\frac{1}{2}} + \delta_x(v_z)^{n+\frac{1}{2}}_{l_x+\frac{1}{2},l_y,l_z+\frac{1}{2}} \right] \\
\delta_t(\tau_{yz})^{n+\frac{1}{2}}_{l_x,l_y+\frac{1}{2},l_z+\frac{1}{2}} = \mu_{l_x,l_y+\frac{1}{2},l_z+\frac{1}{2}} \left[\delta_z(v_y)^{n+\frac{1}{2}}_{l_x,l_y+\frac{1}{2},l_z+\frac{1}{2}} + \delta_y(v_z)^{n+\frac{1}{2}}_{l_x,l_y+\frac{1}{2},l_z+\frac{1}{2}} \right]
\end{cases} \tag{3}$$

In the equation, the superscript denotes the time step, and the subscript denotes the spatial node.

The stress and velocity components in the equations are updated iteratively at each time step. Initially, both velocity and stress components are set to zero. To ensure algorithm stability and minimize numerical dispersion, the spatial and temporal step sizes must satisfy the following conditions in three dimensions:

$$\frac{\Delta t \, v_{\max}}{\Delta x} \le \left(\sqrt{3} \sum_{m=0}^{N-1} |a_m| \right)^{-1} \tag{4}$$

In the equation, Δt is the time step, Δx is the spatial step, and the spatial order is $2N$; m is the coefficient index.

To eliminate spurious reflections from artificial truncation boundaries, a non-splitting Convolutional Perfectly Matched Layer

Table 1
Coefficients for the SGFD approximation.

Spatial order 2N	m	a_m
2	0	1
4	0	9/8
	1	−1/24
6	0	75/64
	1	−25/384
	2	3/640

(CPML) is applied at all boundaries (Zhao et al., 2007). Building on this algorithm, a FD acoustic wavefield simulation program was developed, incorporating OpenMP-based multithreading to improve computational efficiency (Yang et al., 2018). Finally, horizontal well formation models were constructed, and numerical simulations of acoustic logging were performed.

2.2. Verification of the FD algorithm in acoustic logging

The numerical accuracy of the FD algorithm was validated by comparing monopole waveforms generated in isotropic media with benchmark solutions obtained using the Real-Axis Integration (RAI) technique.

As shown in Fig. 2, the isotropic formation borehole model measures 2.2 m × 1.0 m × 1.0 m, with a grid spacing of 0.0025 m and a time step of 0.18 μs. A 30-grid CPML is implemented at each boundary to suppress spurious reflections. The borehole, with a radius of 0.1 m, is filled with water. The transmitter-receiver (TR) spacing is set to 1.5 m. The excitation signal is a Ricker wavelet with a time delay of 0.15 ms and a dominant frequency of 10 kHz. The formation material properties of model were listed in Table 2.

As illustrated in Fig. 3, the excellent agreement between the RAI and FD solutions—including matching phase characteristics, highly consistent amplitude profiles, and reliable wave mode identification—not only validates the numerical accuracy but also confirms the reliability of our finite-difference implementation.

Table 2
Material properties used in the anisotropic formation model.

Material properties	V_p, m/s	V_s, m/s	ρ, kg/m^3
Formation	4000	2300	2200
Borehole fluid	1500		1000

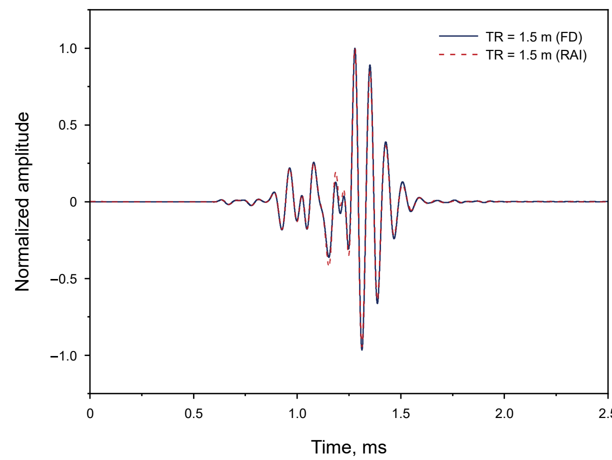

Fig. 3. Comparison of waveforms computed using the FD and RAI methods.

3. Numerical investigation of formation interface effects on horizontal borehole wave modes

When the formation interface is parallel to the borehole axis, the first-arrival time of the waveform matches the P-wave travel time in the fast formation (Cong and Qiao, 2008). Building on this, a borehole embedded in a slow formation, which is surrounded by a fast formation is considered, and the wave mode responses are systematically investigated as the interface location varies.

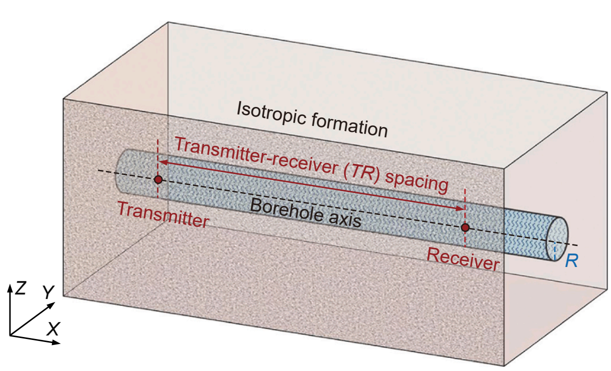

Fig. 2. Schematic of the isotropic formation model with a borehole.

3.1. Horizontal well formation model with an interface

Fig. 4 exhibits a horizontal borehole model with a formation interface. the numerical model measures 2.2 m × 0.8 m × 1.0 m, with a grid spacing of 0.0025 m and a time step of 0.11 μs. A 30-grid-thick CPML is applied to suppress spurious reflections. The borehole has a radius of 0.1 m and is filled with water. To investigate the effect of the formation interface, the interface–borehole distance (L) is varied from 0.15 m to 0.75 m in 0.05 m increments, resulting in a total of 13 distinct models. The material properties of the formations used in the simulations are listed in Table 3. Material property slices in the YZ plane for different models were

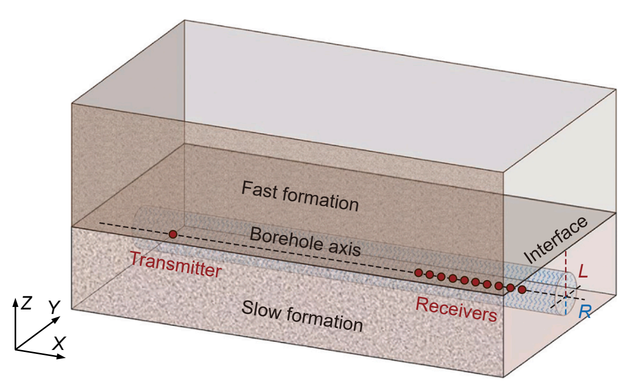

Fig. 4. Horizontal borehole model with a formation interface.

Table 3
Material properties used in the two-layer formation model.

Material properties	V_p, m/s	V_s, m/s	ρ, kg/m^3
Fast formation	6350	3450	2710
Slow formation	4000	2300	2200
Borehole fluid	1500		1000

generated (Fig. 5) to verify the correctness of material property assignments and formation interface positions.

Numerical simulations were performed using the above models. A monopole transmitter and a linear array of ten receivers are used in the simulations. The minimum TR spacing is set to 1.0 m, and the receiver-to-receiver spacing is 0.1 m. This generalized single-source-multi-receiver geometry is adopted to provide sufficient offset sampling for analyzing the first-arrival response and borehole wave mode responses. The source signal is a Ricker wavelet with a time delay of 0.15 ms and a dominant frequency of 10 kHz (Su et al., 2022). The recorded signals are the time-domain full-waveforms of the stress response at each receiver location. The analytical form of the Ricker wavelet is shown in Eq. (5) and the source and recorded waveforms are shown in Fig. 6.

$$s(t) = \left[1 - 2\pi^2 f_0^2 (t - t_0)^2\right] \mathrm{e}^{\left[-\pi^2 f_0^2 (t-t_0)^2\right]} \tag{5}$$

In the equation, f_0 is the dominant frequency and t_0 is the time delay.

Fig. 6(a) illustrates the source waveform generated using Eq. (5), while Fig. 6(b) shows the recorded array acoustic full-waveforms simulated using the FD method for L= 0.30 m model. We extracted three key attributes: propagation velocities (V_p, V_s), relative energy amplitudes, and dominant frequencies of P- and S-wave modes. These parameters enable a comprehensive investigation of the effects of formation interface position on acoustic propagation characteristics.

3.2. Velocity response to formation interfaces

Waveforms from adjacent receivers were grouped into overlapping three-receiver sets (TR1.0–TR1.1–TR1.2, TR1.1–TR1.2–TR1.3, …) to construct a series of single-transmitter, three-receiver datasets. P- and S-wave velocities were then extracted using the slowness-time coherence (STC) method. For each three-receiver set, the STC-derived velocity was assigned to the midpoint TR spacing (Fig. 7(a)), for example, the velocity obtained from TR1.0–TR1.1–TR1.2 array data represents the value at TR = 1.1 m. This approach enhances the stability of the velocity estimates while preserving the TR resolution, enabling velocity variations to be examined with respect to both L and TR spacing.

The comprehensive results are presented in Fig. 7(b), where each curve represents a TR spacing, and the results from multilayer models are distinguished by different line styles, colors, and symbols. As shown in the figure, when L is small, the measured P-wave velocity in the borehole is approximately 6100 m/s (close to the P-wave velocity of the fast formation). As L increases, the P-wave velocity gradually decreases and then stabilizes at 4000 m/s (close to the P-wave velocity of the slow formation). Furthermore, the L corresponding to the velocity transition increases with TR.

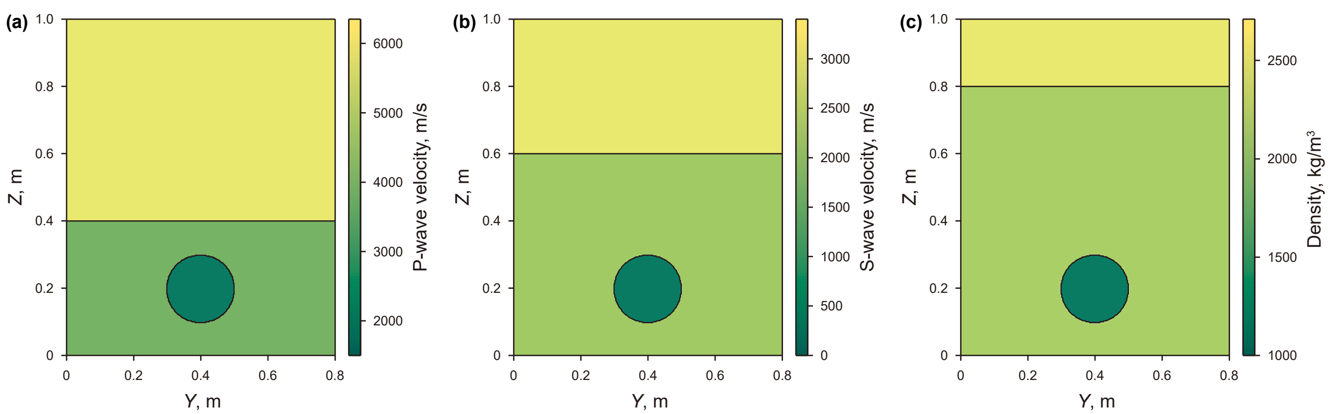

Fig. 5. Material property slices for different interface–borehole distances. **(a)** P-wave velocity slice for the L= 0.20 m model; **(b)** S-wave velocity slice for the L= 0.40 m model; and **(c)** density slice for the L= 0.60 m model.

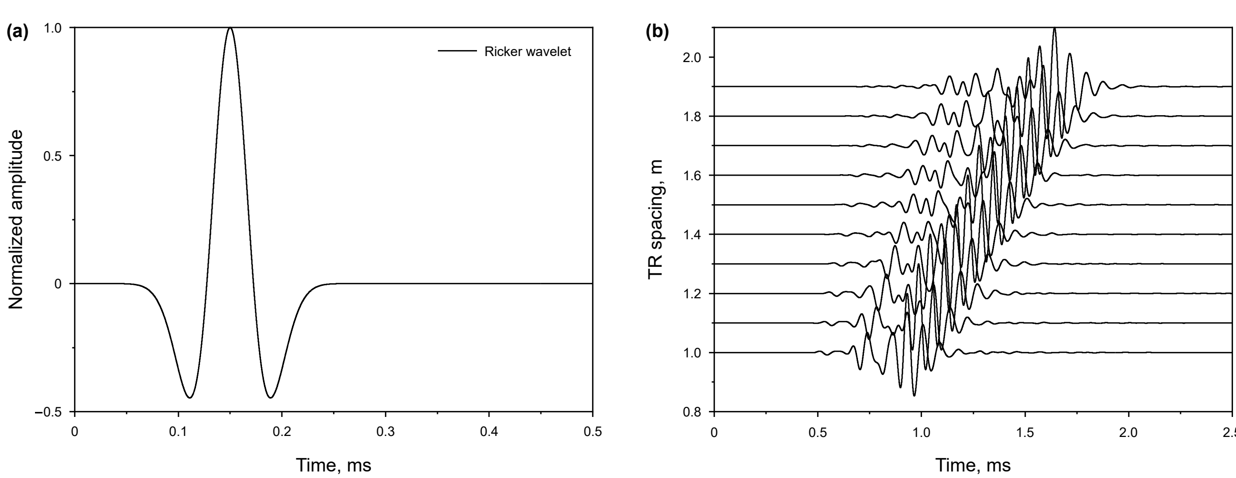

Fig. 6. Source and recorded signals used in the simulations. **(a)** Ricker wavelet source signature (f_0= 10 kHz, t_0= 0.15 ms); and **(b)** simulated full-waveforms of the stress response recorded by the receiver array (L= 0.30 m).

This demonstrates that the investigation depth of the P-wave in acoustic logging increases with TR spacing. Conversely, the S-wave velocity remains stable approximately 2300 m/s (close to the S-wave velocity of the slow formation). This stability indicates that the S-wave exhibits minimal response to variations in *L* values.

To better visualize the variations of characteristic parameters with *L* and TR, we performed two-dimensional interpolation of the parameter array in the TR–*L* domain and represented the results using a color scale. This visualization is referred to as the TR–*L* spectrum.

Fig. 7(c) shows the TR–*L* spectrum of P-wave velocity. The spectrum exhibits a distinct linear boundary separating the high-velocity (yellow) and low-velocity (blue) regions, indicating a linear relationship between P-wave investigation depth and TR spacing. The TR–*L* spectrum of S-wave velocity in Fig. 7(d) shows no distinct variation pattern with TR or *L*. In summary, the formation interface exerts a significant influence on P-wave velocity but has negligible effect on S-wave velocity.

3.3. Energy response to formation interfaces

The first-arrivals of P- and S-waves are used to determine the start positions of the time windows. Each wave mode segment, with a window length of 1.5 periods, is extracted from the full-wave signal (Fig. 8). The energy of each wave mode segment within the window is calculated according to Eq. (6), by accounting for the contribution of each sample point.

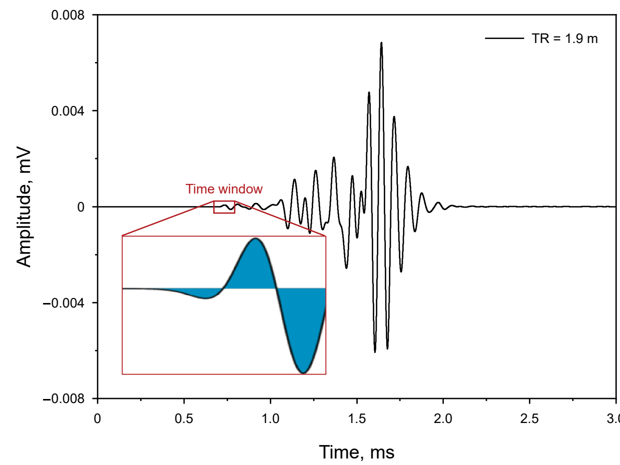

Fig. 8. Schematic of the wave mode segment extracted by a time window.

$$E = \left(\sum_{i=1}^{n} A_i^2\right) \cdot n^{-1} \tag{6}$$

In the equation, *E* is the energy, *A* is the amplitude, *n* is the sample point number of the waveform in the windows, and *i* is the sample point index.

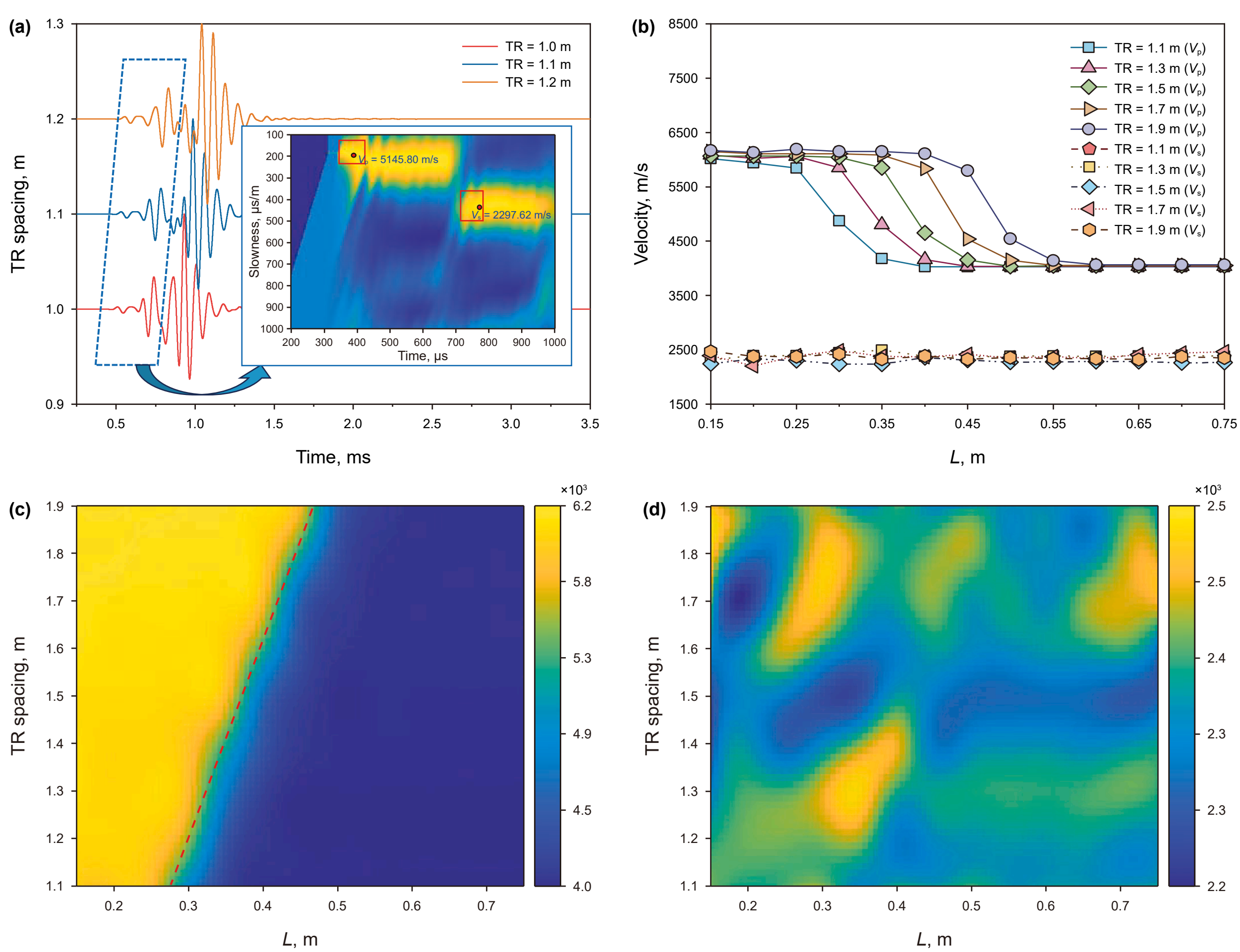

Fig. 7. Wave mode velocity dependence on *L* and TR spacing. **(a)** STC spectrum of single-source three-receiver waveforms (TR = 1.0, 1.1, and 1.2 m); **(b)** velocity variations versus *L* at different TR spacings; **(c)** TR–*L* spectrum of P-wave velocity; and **(d)** TR–*L* spectrum of S-wave velocity.

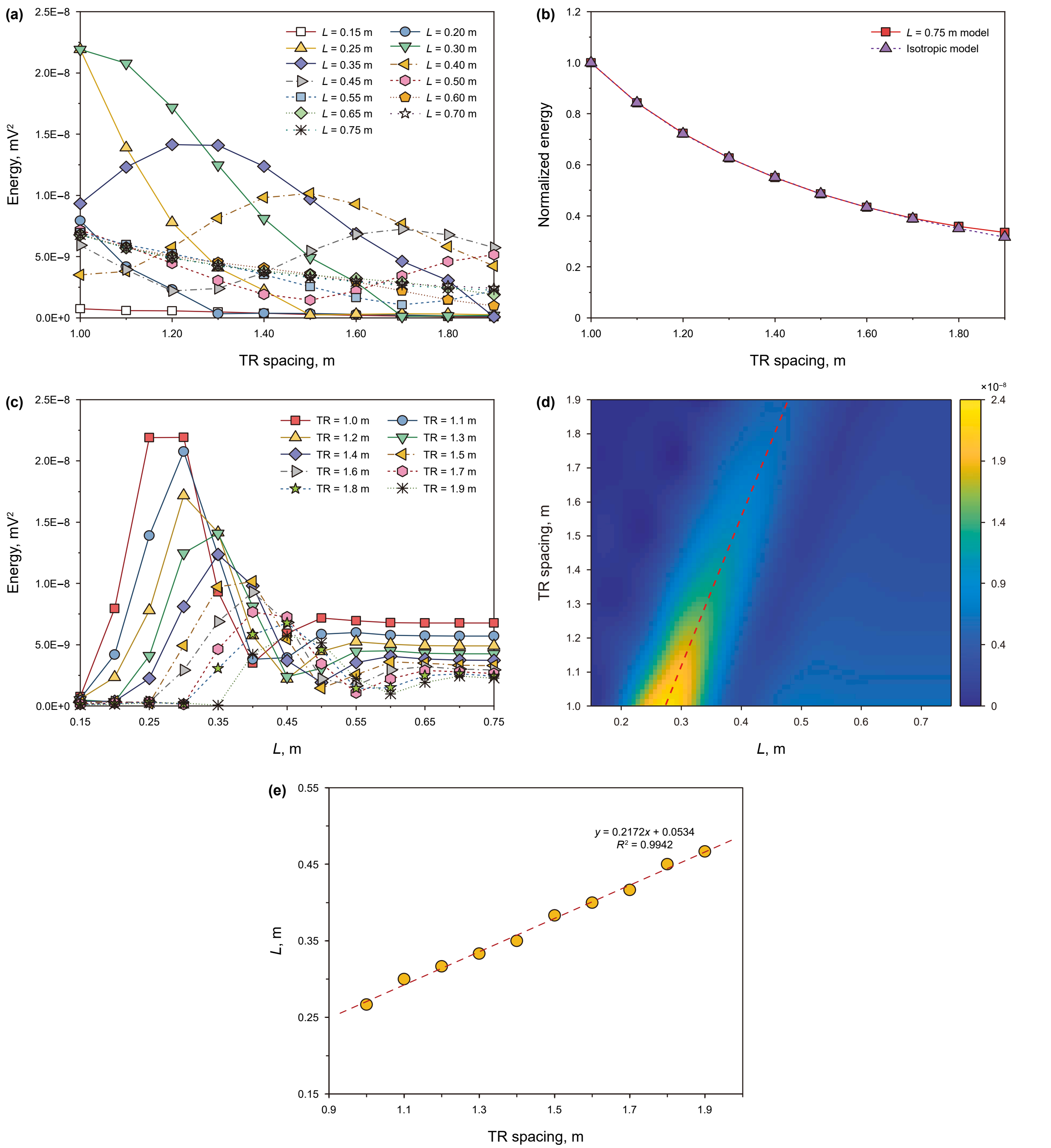

Fig. 9. P-wave energy dependence on TR spacing and *L*. **(a)** Energy decay for models with different *L* values; **(b)** comparison between the *L*= 0.75 m model and the isotropic model; **(c)** variation of energy with *L* at different TR spacings; **(d)** TR–*L* spectrum of P-wave energy; and **(e)** fitted relationship between TR spacing and *L* at the spectrum peak.

We extracted the P-wave and S-wave energies at each TR spacing from models with varying *L* values. This yields the energy–TR relationships for both wave modes across all models. In homogeneous isotropic formations, the energies of P- and S-waves typically decay exponentially with increasing TR spacing (Tang and Cheng, 2004).

However, the adjacent formation interface alters the energy decay behavior in horizontal wells, resulting in a deviation from the exponential trend. Fig. 9 shows the variation of P-wave energy with TR spacing and *L*. Fig. 9(a) reveals a non-monotonic variation of P-wave energy as a function of TR spacing, characterized by an initial increase followed by decay, forming a distinct peak. The peak position systematically shifts toward larger TR values as *L* increases. Meanwhile, the peak feature gradually diminishes, and the energy decay becomes monotonic, eventually approaching the exponential decay characteristic of homogeneous media. As shown in Fig. 9(b), the P-wave energy decay for the *L*= 0.75 m model (red curve) closely matches that of the isotropic model

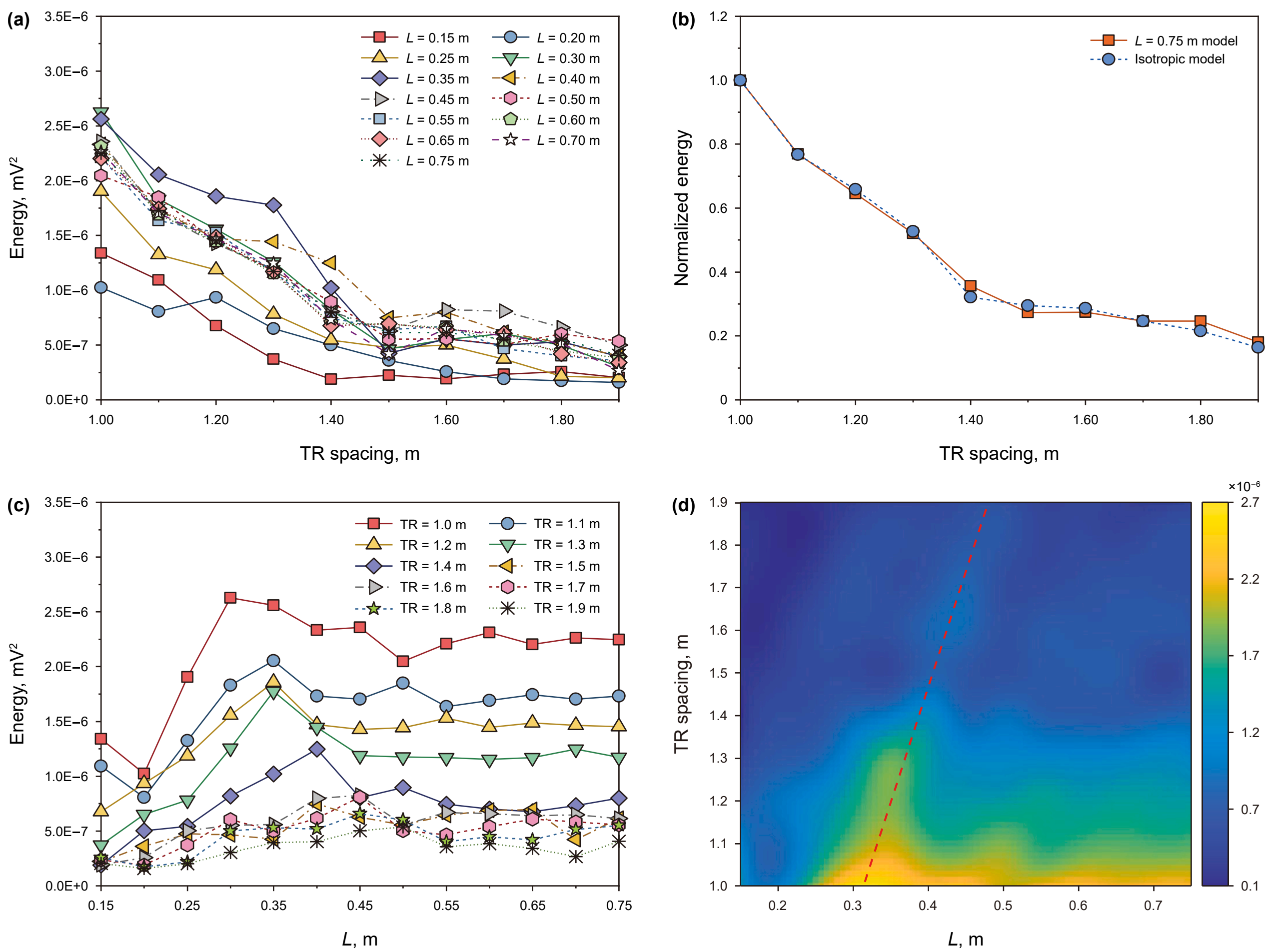

Fig. 10. S-wave energy dependence on TR spacing and *L*. **(a)** Energy decay for models with different *L* values; **(b)** comparison between the *L*= 0.75 m model and the isotropic model; **(c)** variation of energy with *L* at different TR spacings; and **(d)** TR–*L* spectrum of S-wave energy.

(purple curve). Fig. 9(c) shows the variation of P-wave energy with *L* for different TR spacings, with each curve representing a specific TR spacing. The figure indicates that each curve exhibits an energy peak, which shifts along the *L*-axis as TR increases. Fig. 9(d) presents the TR–*L* spectrum of P-wave energy, with color representing the energy magnitude. The spectrum peak exhibits a clear linear TR–*L* relationship. Fig. 9(e) illustrates the linear fit between TR and *L* at the spectrum peak, with the fitted relationship given in Eq. (7).

$$L = 0.2172 \cdot \mathrm{TR} + 0.0534 \; R^2 = 0.9942 \tag{7}$$

In the equation, *L* is the distance from the formation interface to the borehole axis, TR is the transmitter-receiver spacing, and R^2 is the coefficient of determination.

Fig. 10 illustrates the S-wave energy variation pattern with increasing TR spacing and varying *L* values. As shown in Fig. 10(a), when $L < 0.50$ m, the formation interface at different positions affects the S-wave energy decay and induces fluctuations in the decay curve. However, the overall trend still follows an exponential decay. When $L > 0.50$ m, the fluctuations in the S-wave energy decay curve diminish. The decay trend stabilizes and gradually approaches the exponential behavior characteristic of an isotropic medium. As shown in Fig. 10(b), the S-wave energy decay trend for the $L = 0.75$ m model (orange curve) closely matches that of the isotropic medium (blue curve). In Fig. 10(c), the S-wave also shows an energy peak similar to that of the P-wave, though less pronounced. Meanwhile, the peak gradually shifts along the *L*-axis with increasing TR. Fig. 10(d) faintly exhibits a general linear trend in the S-wave energy TR–*L* spectrum.

In summary, the formation interface significantly affects P-wave energy, while its effect on S-wave energy is comparatively weaker. A plausible contributing factor is that the refracted S-wave (shear head wave) energy is more concentrated near the borehole wall, implying a shallower effective investigation depth; therefore, the S-wave energy response to an external formation interface may be weaker and less distinguishable than that of the P-wave (Wang et al., 2020). Building on these results, we propose a first-arrival-based interface detection concept: the interface position can be inferred by exploiting the quantitative relationship between the P-wave energy peak, the interface distance, and the TR spacing. However, this detection method is exclusively applicable to near-borehole configurations in which the borehole is located in a slower formation adjacent to a faster outer formation (i.e., $V_{\mathrm{p,\ out}} > V_{\mathrm{p,\ in}}$). For the reversed velocity contrast ($V_{\mathrm{p,\ out}} < V_{\mathrm{p,\ in}}$), the first-arrival becomes weakly sensitive to the outer slower formation, the method is no longer suitable for such scenarios.

3.4. Frequency response to formation interfaces

To examine the influence of formation interfaces on wave mode frequency characteristics, we extracted the dominant frequencies of P-waves and S-waves. First, the wave segments (Fig.

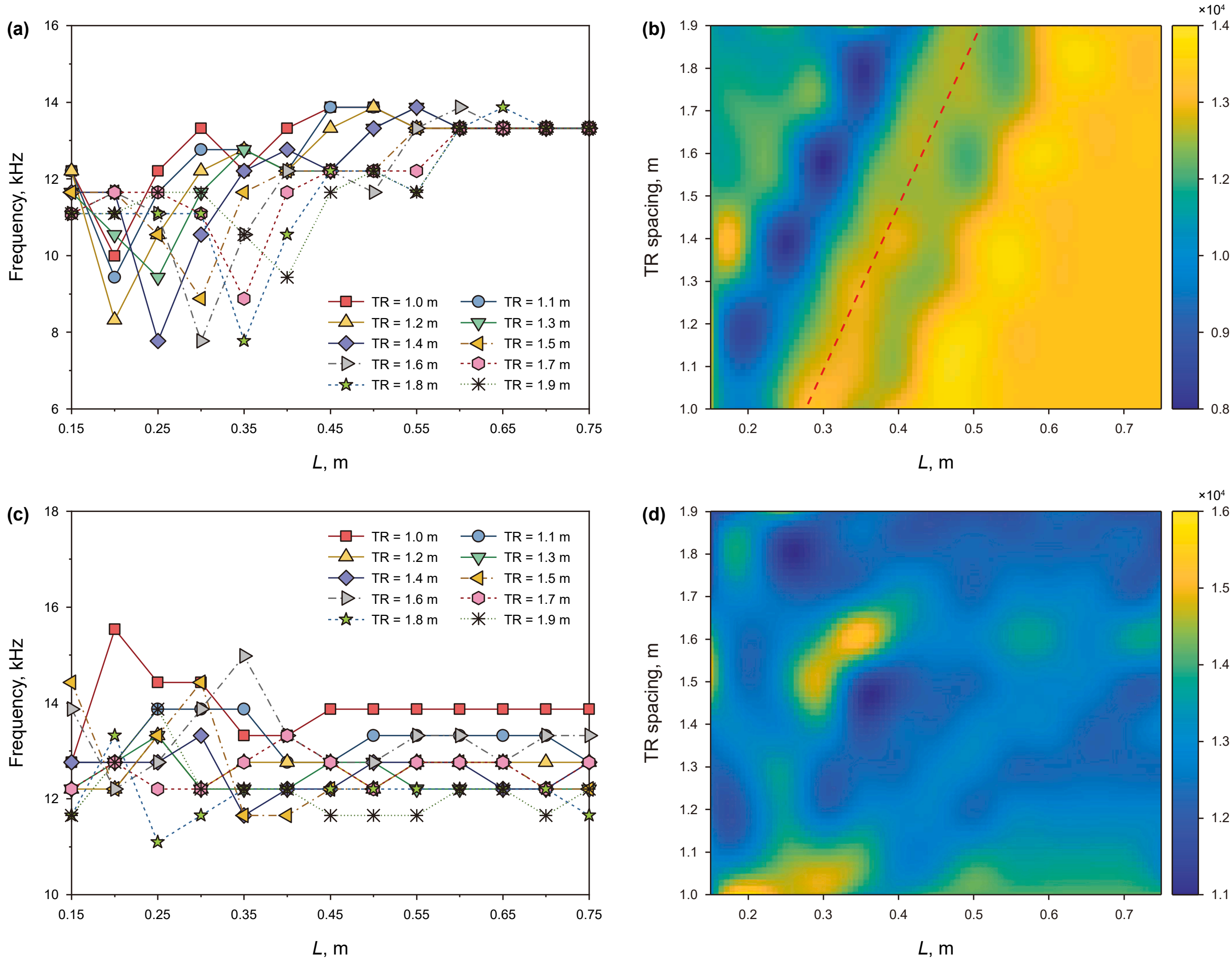

Fig. 11. Wave mode dominant frequency dependence on TR spacing and *L*. **(a)** Variation of P-wave frequency with *L* at different TR spacings; **(b)** TR–*L* spectrum of P-wave frequency; **(c)** variation of S-wave frequency with *L* at different TR spacings; and **(d)** TR–*L* spectrum of S-wave frequency.

8) were windowed using a Hann function. The segments were then zero-padded to an appropriate length. Subsequently, the extended waveform segments were transformed into the frequency domain using FFT. The dominant frequency of each wave mode was determined by identifying the frequency at the half-power point of its spectrum. The relationship between the dominant frequencies of P- and S-waves and *L* and TR spacing is shown in Fig. 11.

Fig. 11(a) shows the variation of P-wave dominant frequency with *L* for different TR spacings. Each curve, distinguished by color, represents the P-wave frequency for a specific TR spacing. The P-wave dominant frequency exhibits a distinct oscillatory behavior caused by the formation interfaces. For small *L*, the P-wave frequency is relatively low, around 11 kHz. As *L* increases, the frequency gradually rises while exhibiting oscillations. When *L* exceeds a threshold, the dominant frequency stabilizes at approximately 13 kHz. This phenomenon is more clearly observed in the P-wave dominant frequency TR–*L* spectrum (Fig. 11(b)), which exhibits distinct color bands and a clear linear relationship between *L* and TR. Fig. 11(c) shows the relationship between the S-wave dominant frequency and *L* for different TR spacings. The S-wave frequency oscillates primarily between 11 and 15.5 kHz, exhibiting no clear correlation with *L* variations. The S-wave dominant frequency TR–*L* spectrum in Fig. 11(d) also shows no distinct variation pattern with *L* or TR spacing.

In summary, the formation interface exerts a significant influence on the P-wave dominant frequency, whereas its impact on the S-wave dominant frequency is relatively minor.

4. Mechanism analysis of formation interface effects on wave modes

Building on the previous findings, the formation interface exerts a more significant influence on P-wave characteristics than on S-wave characteristics. To elucidate the underlying physical mechanisms, we analyzed *XZ*-plane stress wavefield snapshots at successive propagation times (t) across models with varying L values. The grayscale visualizations of stress wave intensity illustrate how P-wave propagation dynamics evolve with interface proximity and wavefront advancement. Analysis of wavefield patterns under different (L, t) conditions reveals how interface interactions govern P-wave behavior in the borehole environment.

4.1. Influence mechanism of horizontal interfaces

Fig. 12 presents wavefield snapshots at $t = 0.534$ ms for two-layer models with different L values. After being excited by the transmitter, elastic waves propagate through the borehole wall and the slow formation before reaching the fast formation. This process produces two distinct types of P-waves (red and blue

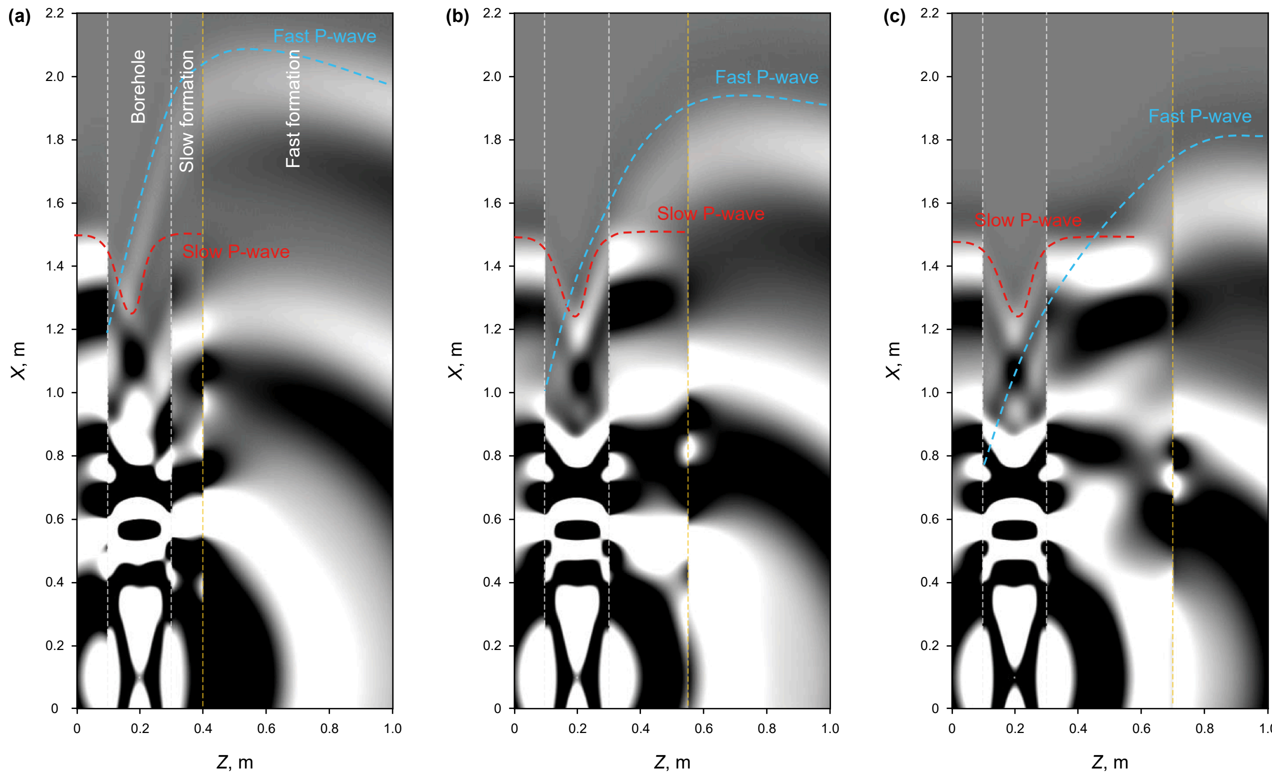

Fig. 12. Wavefield snapshots at $t = 0.534$ ms for models with different interface–borehole distances (L). **(a)** $L = 0.20$ m; **(b)** $L = 0.35$ m; and **(c)** $L = 0.50$ m.

curve). The first are slow refracted P-waves generated at the borehole wall by waves propagating through the slow formation. The second are fast refracted P-waves formed at the formation interface by waves in the fast formation, which subsequently generate secondary fast refracted waves at the borehole wall. For clarity, these are referred to as slow P-waves and fast P-waves, respectively. Both wave types are eventually detected within the borehole, and their relative arrival times and amplitudes provide critical information about the formation interface position.

Fig. 12(a) shows the stress wavefield for the model with $L = 0.20$ m. At this time, the first-arrival recorded in the borehole corresponds to the fast P-wave excited from the fast formation on one side. In the grayscale image, this waveform appears in light gray, indicating a relatively low amplitude. Fig. 12(b) shows the wavefield for the model with $L = 0.35$ m. At this time, the fast and slow P-waves overlap in the borehole, coinciding at the first-arrival. The wavefield exhibits a marked increase in grayscale intensity at the overlap point, indicating that the in-phase superposition of the two waves leads to significant amplitude enhancement. Additionally, slight variations in the widths of the light and dark bands at the first-arrival suggest a phase shift between the overlapping waveforms, potentially causing fluctuations in the dominant frequency. Fig. 12(c) shows the wavefield for the model with $L = 0.50$ m. At this time, the first-arrival in the borehole corresponds to the slow P-wave propagating from the slow formations on both sides. Its waveform appears more prominent than that of the fast P-wave, reflecting a higher signal amplitude at the first-arrival.

A receiver is placed at 1.4 m along the X-axis, and P-wave segments at TR = 1.3 m are extracted for various L values to compare the trends in velocity, energy, and dominant frequency. Fig. 13 exhibits the variations in P-wave characteristic parameters with L at TR = 1.3 m, the extraction procedure of the first-arrival segments is described in Section 3.3.

Fig. 13(a) shows the P-wave segments for different L values at TR = 1.3 m. The axes represent the time and amplitude of the P-wave segment at $L = 0.35$ m. The remaining curves are vertically and horizontally offset. Based on the arrival time, amplitude, and dominant frequency of the extracted first-arrival segments, the waveforms are classified as fast and slow P-waves, and the identified types are labeled in figure for clarity. Noticeable amplitude variations, peak splitting, and waveform broadening are observed, indicating corresponding variations in both the energy and dominant frequency of P-waves as L increases.

Fig. 13(b) shows the variation in normalized P-wave velocity, energy, and dominant frequency with L at TR = 1.3 m. In figure, the green, blue, and yellow curves represent normalized velocity, energy, and dominant frequency, respectively. When $L < 0.25$ m, the first-arrival velocity corresponds to that of the fast P-wave. In this range, P-wave energy remains relatively low, and the dominant frequency is nearly constant. At $L = 0.35$ m, the first-arrival velocity lies between the fast and slow P-wave velocities. P-wave energy reaches its maximum, and notable fluctuations in dominant frequency are observed on either side of this location. These variations indicate the overlap of the two wave modes at this moment. When $L > 0.45$ m, the first-arrival corresponds to the slow P-wave. In this range, the P-wave energy remains relatively high, and the dominant frequency gradually stabilizes. Additionally, near $L = 0.25$ m and 0.45 m, a reduction in dominant frequency accompanied by an increase in energy suggests interference between the fast and slow P-waves. This interpretation is supported by the peak splitting ($L = 0.25$ m) and waveform broadening ($L = 0.45$ m) observed in Fig. 13(a). Mode conversion between the two wave types occurs within this interval. Fig. 13(c) presents the P-wave mode conversion interval for TR = 1.1–1.9 m. Across different TR spacings, the P-wave characteristic parameters exhibit consistent trends with L. However, the L thresholds used to distinguish the first-arrival components are

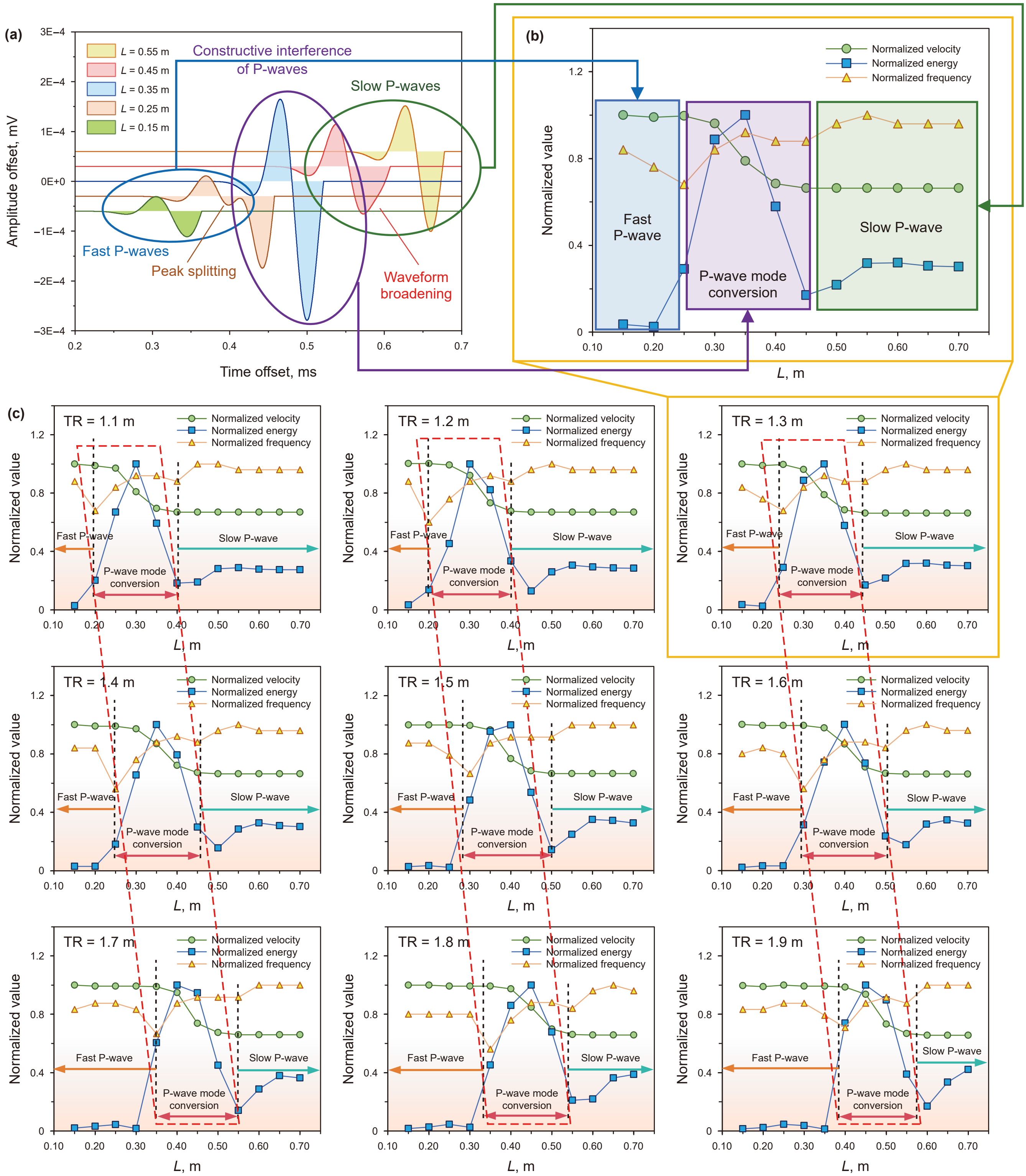

Fig. 13. Variation of P-wave characteristic parameters with L. **(a)** P-wave segment stacking diagram for different L values at TR = 1.3 m; **(b)** comparison of normalized P-wave characteristic parameters at TR = 1.3 m; and **(c)** P-wave mode conversion range of different TR spacings.

TR-dependent and increasing in a near-linear trend as the TR spacing increases. This phenomenon is consistent with the results observed in the wavefield snapshots.

The above analytical results are consistent with the wavefield snapshot observations, providing mutual validation for the wave mode response characteristics. To further investigate the conversion mechanism between fast and slow P-waves, wavefield snapshots of the model with $L = 0.30$ m at various time steps are shown in Fig. 14.

At $t = 0.406$ ms, the slow P-wave constitutes the first-arrival in the borehole (Fig. 14(a)). At $t = 0.502$ ms (Fig. 14(b)), the fast P-wave overtakes the slow P-wave, and the two overlap, jointly

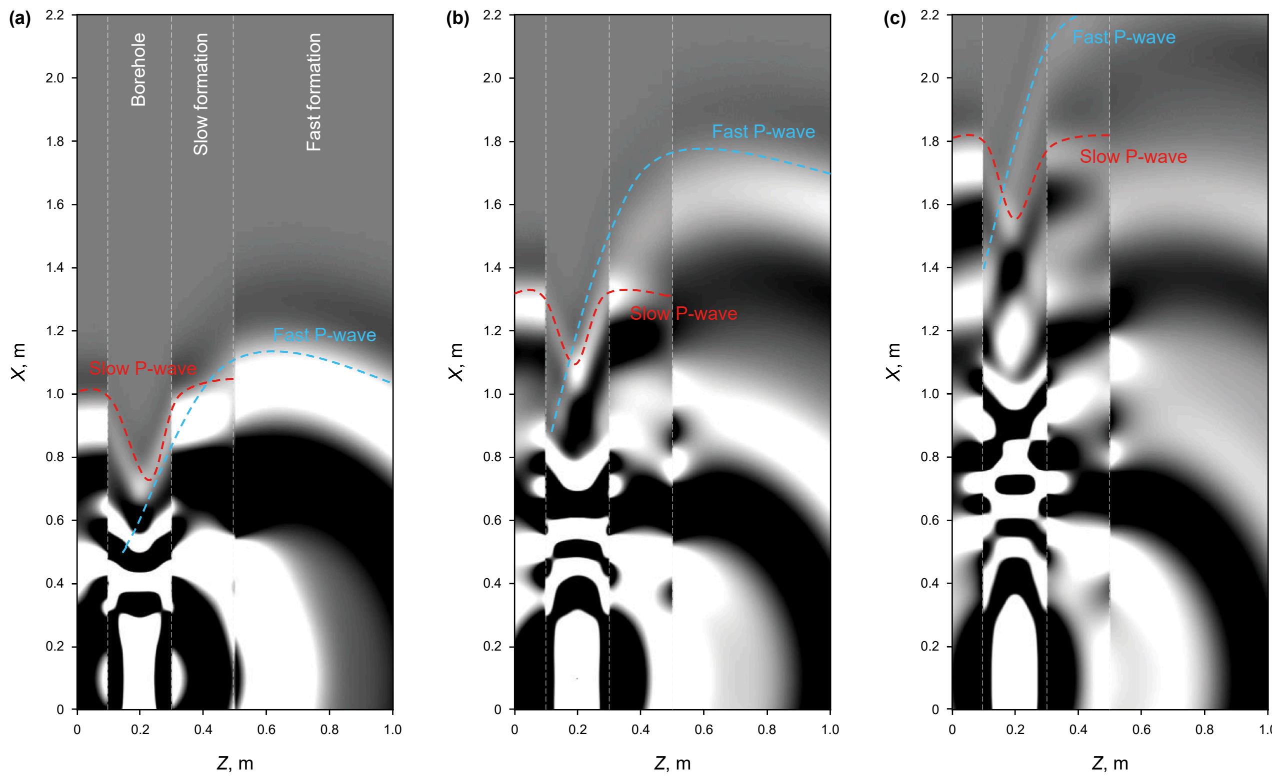

Fig. 14. Wavefield snapshots of the $L = 0.30$ m model at different time steps (t). **(a)** $t = 0.406$ ms; **(b)** $t = 0.502$ ms; and **(c)** $t = 0.614$ ms.

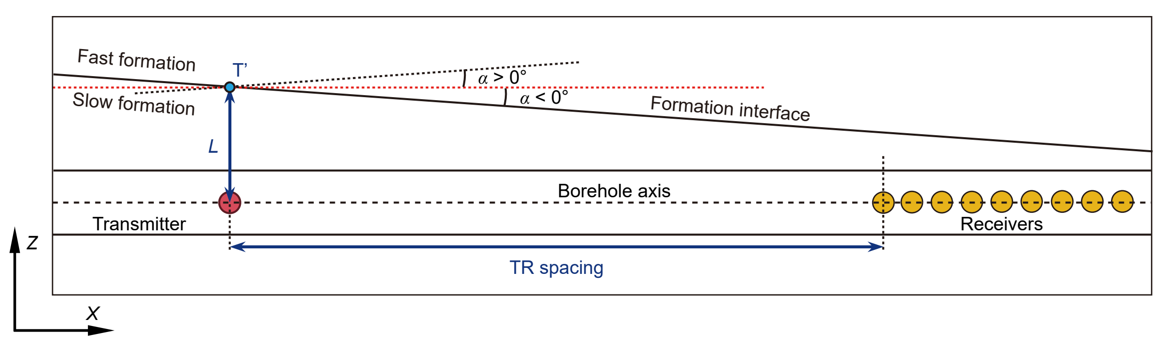

Fig. 15. Schematic of the borehole model with an inclined formation interface.

constituting the first-arrival. At $t = 0.614$ ms (Fig. 14(c)), the fast P-wave completely overtakes the slow P-wave and becomes the dominant component of the first-arrival.

This suggests that even within a single model, the first-arrival composition evolves over time. With increasing propagation time, the fast P-wave gradually overtakes the slow P-wave and becomes the first-arrival in the borehole. Consequently, the slow P-wave is mainly observed at near-receiver positions, whereas the fast P-wave dominates at larger offsets.

4.2. *Influence mechanism of small-angle dipping interfaces*

A small dip angle is assumed for the formation interface, and the interface is fixed near the borehole and does not intersect the borehole, as shown in Fig. 15. The distance from the transmitter to the interface in the Z direction is fixed at $L = 0.40$ m. The formation is rotated about point T', and the dip angle (α) is set to $-6°$, $-4°$, $-2°$, $0°$, $2°$, $4°$, and $6°$. The model extends to 2.6 m in the X direction, and the minimum receiver offset is set to 0.8 m. All other parameters remain identical to those used in the horizontal-interface model.

Fig. 16 shows wavefield snapshots at $t = 0.566$ ms for inclined-interface models with different dip angles. The snapshots indicate that, at a fixed L, the interface dip angle affects the timing at which the P-wave first-arrival transition occurs. When $\alpha < 0°$, a larger dip angle leads to an earlier arrival of the fast P-wave, and the first-arrival is the fast P-wave. When $\alpha > 0°$, a larger dip angle delays the arrival of the fast P-wave, and the first-arrival is the slow P-wave.

The P-wave velocity was extracted, and the variation of P-wave velocity with TR for different dip angles is shown in Fig. 17. As indicated in Fig. 17(a), the overall P-wave velocity increases from low to high with increasing TR and finally stabilizes at a high value. However, this overall trend is modulated by the dip angle: When $\alpha < 0°$, a larger dip angle results in a higher stabilized velocity, which can even exceed the fast formation value specified in the model (α

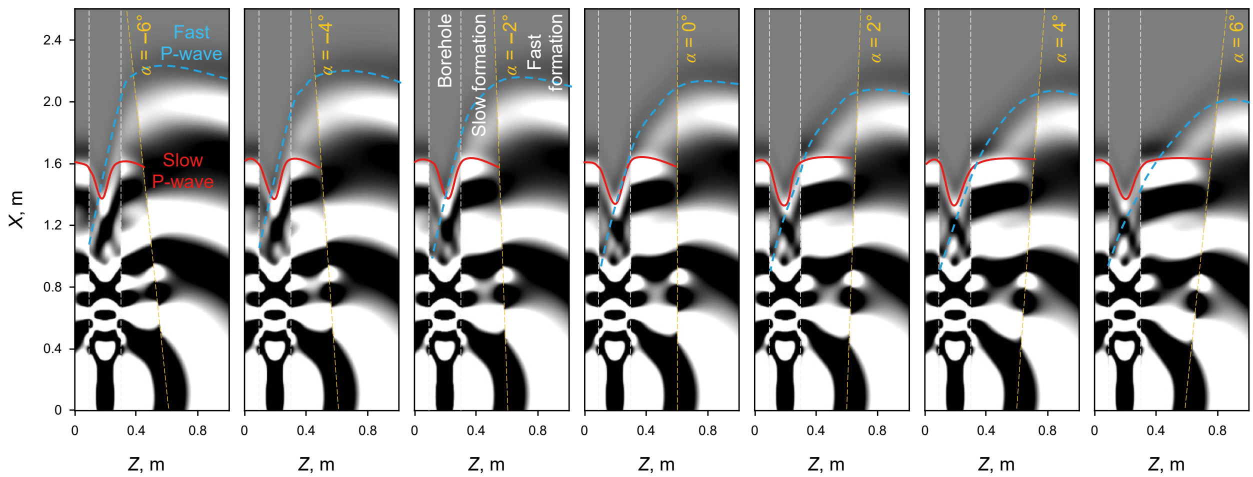

Fig. 16. Wavefield snapshots of the L = 0.40 m model for different interface dip angles (t = 0.566 ms).

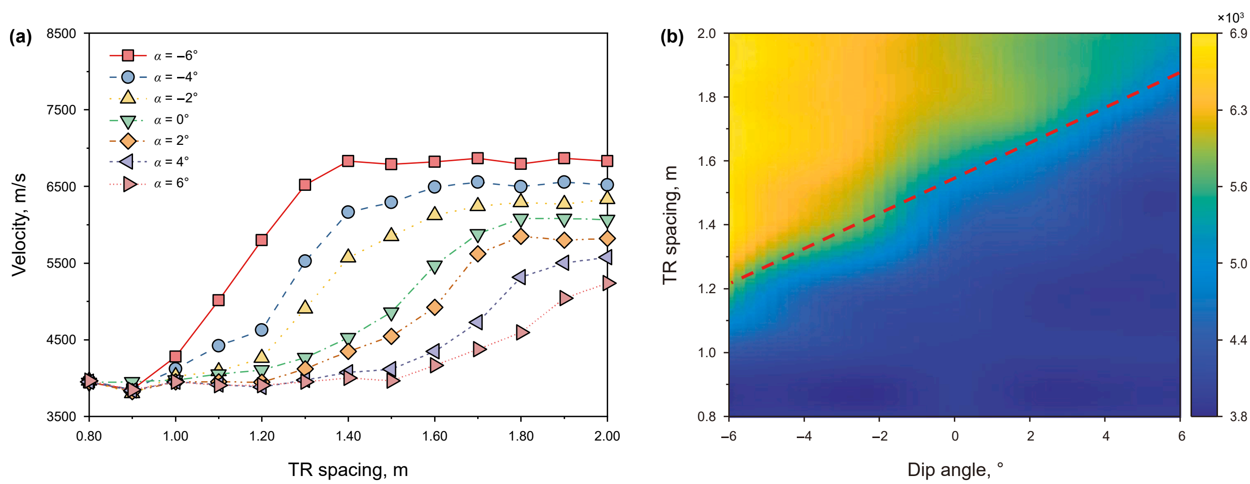

Fig. 17. Variation of P-wave velocity with TR spacing at different dip angles. **(a)** P-wave velocity–TR spacing curves; and **(b)** P-wave velocity TR–angle spectrum.

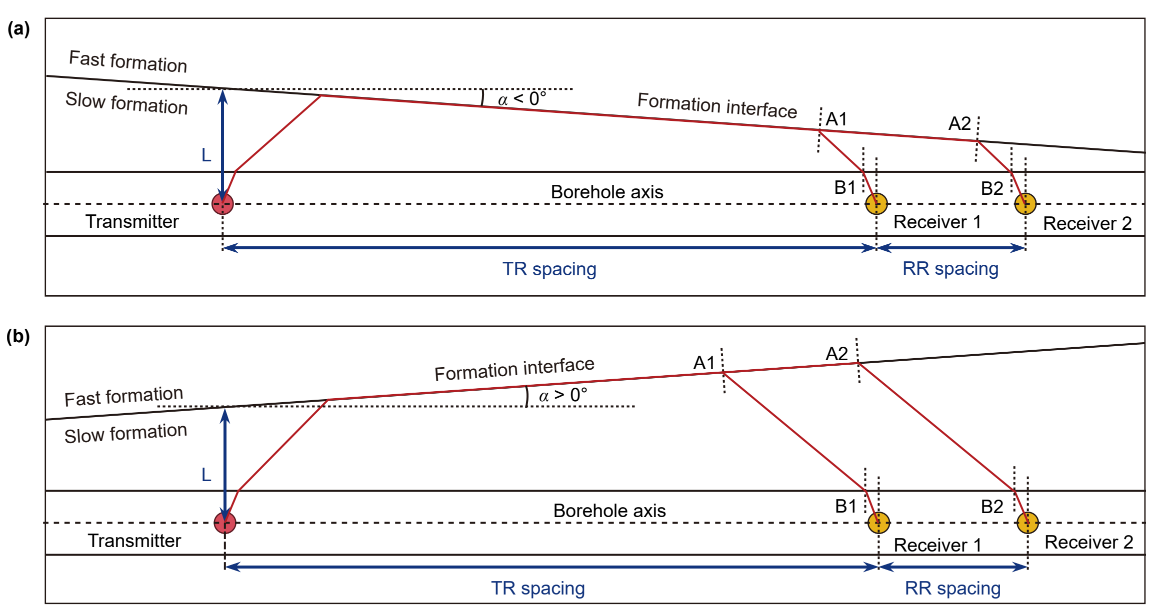

Fig. 18. Interface-controlled P-wave propagation paths for different interface dip angles. **(a)** Negative dip angle (α < 0°); and **(b)** positive dip angle (α > 0°).

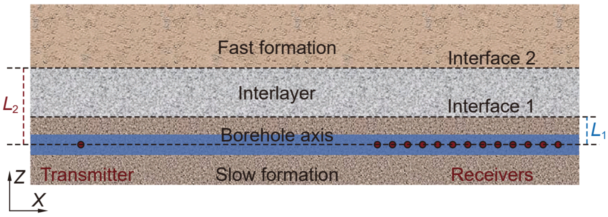

Fig. 19. Schematic of the three-layer formation model with an interlayer.

Table 4
Material properties used in the three-layer formation model.

Material properties	V_p, m/s	V_s, m/s	ρ, kg/m^3
Fast formation	6350	3450	2710
Interlayer	5100	2900	2500
Slow formation	4000	2300	2200
Borehole fluid	1500		1000

$= -6°$, $V_p > 6500$ m/s). When $\alpha > 0°$, a larger dip angle leads to a lower stabilized velocity, falling below the slow formation value specified in the model ($\alpha = 6°$, $V_p < 5500$ m/s).

Fig. 17(b) presents the TR–angle spectrum of P-wave velocity, which is separated into two zones by distinct color bands. The upper yellow zone corresponds to the fast formation velocity, whereas the lower blue zone corresponds to the slow formation velocity. With increasing dip angle, the color in the fast formation zone gradually becomes lighter, indicating that the corresponding velocity decreases as the dip angle increases.

Fig. 18 shows the P-wave propagation paths in the fast formation for different interface dip angles, which account for the velocity deviation discussed above. After excitation by the transmitter, the wave propagates in the borehole fluid and enters the slow formation across the borehole boundary, and then reaches the interface. A head wave (critically refracted P-wave) is generated at the interface and propagates along it at approximately the P-wave velocity of the fast formation. Part of its energy returns from the interface into the slow formation and borehole and is recorded by the receivers. Therefore, the effective path segment from the interface to the borehole boundary near each receiver differs. These two segments are labeled as A1B1 and A2B2 in Fig. 18.

In Fig. 18(a), with $\alpha < 0°$, the interface dip angle leads to A1B1 > A2B2. Therefore, the measured P-wave time difference between the two receivers becomes smaller, resulting in an overestimated velocity. Similarly, in Fig. 18(b), with $\alpha > 0°$, A2B2 > A1B1. The measured P-wave time difference becomes larger, leading to an underestimated velocity. Accordingly, for a near-borehole interface with a small dip angle, mode conversion of the first-arrival still occurs. However, the dip angle can introduce a systematic bias in the estimated velocity of the fast formation. Therefore, the interface dip angle should be explicitly considered in the velocity-correction procedure.

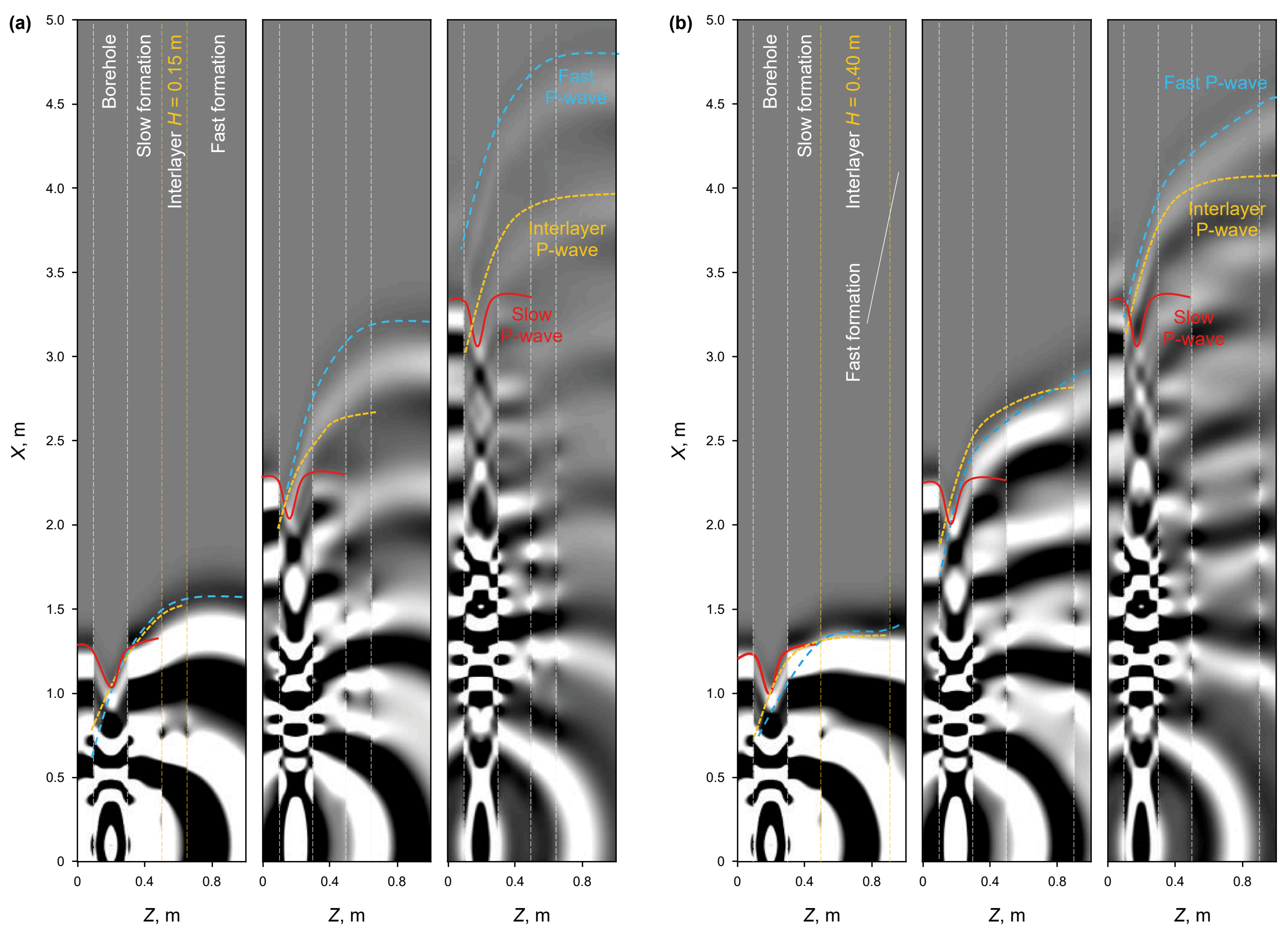

Fig. 20. Wavefield snapshots for models with different interlayer thicknesses (H). **(a)** $H = 0.15$ m; and **(b)** $H = 0.40$ m.

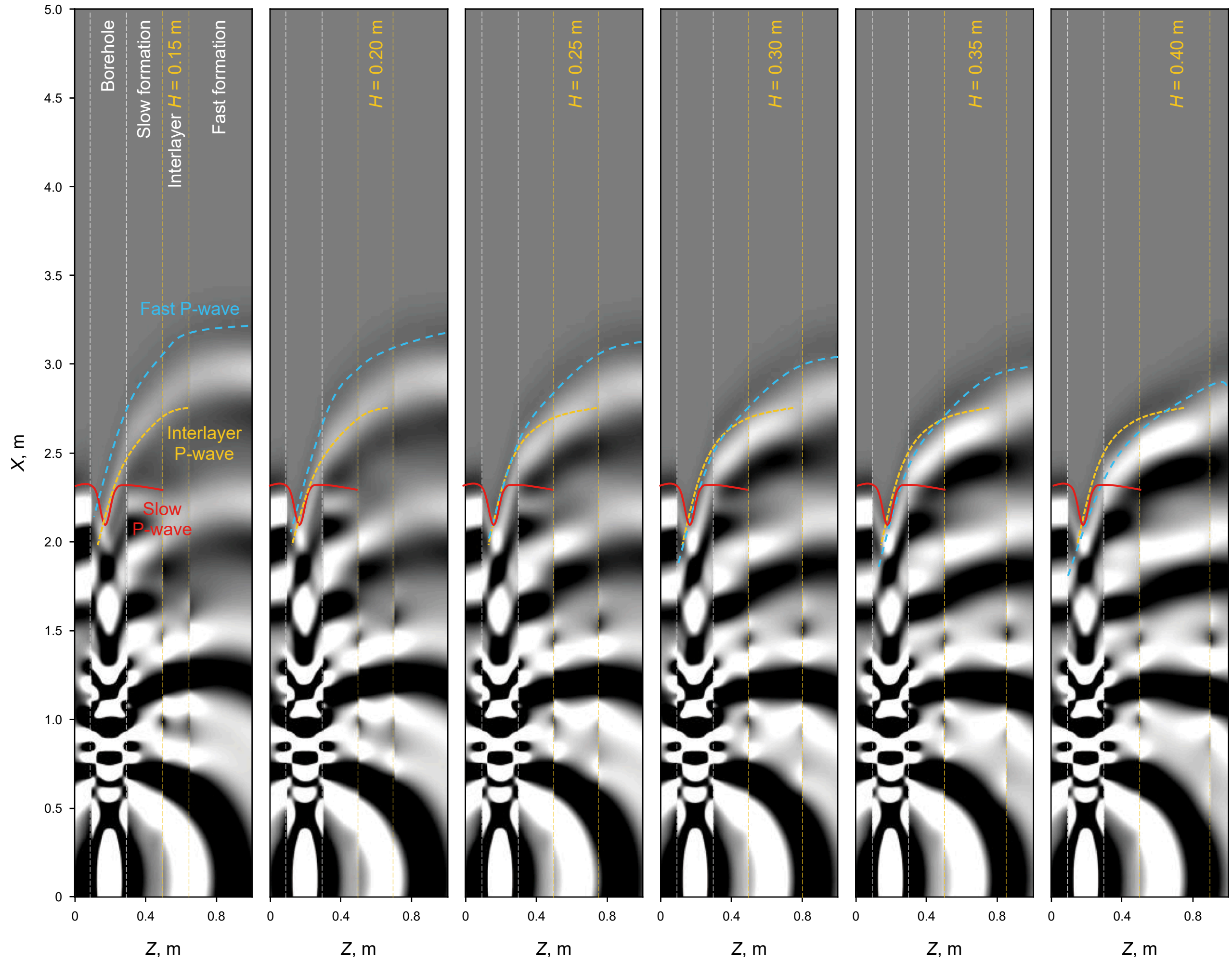

Fig. 21. Wavefield snapshots at $t = 0.727$ ms for models with different interlayer thicknesses (H).

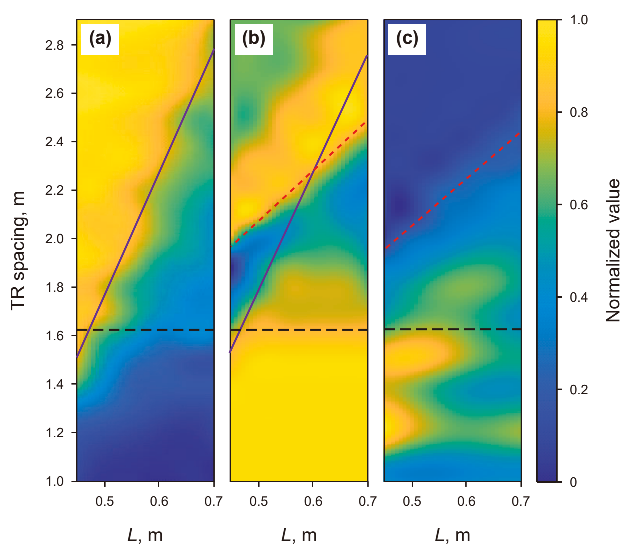

Fig. 22. TR–L spectrum of P-wave parameters. **(a)** Velocity TR–L spectrum; **(b)** frequency TR–L spectrum; and **(c)** energy TR–L spectrum.

In summary, the first-arrival composition in the borehole consistently exhibits a slow-to-fast P-wave transition pattern, observed both temporally within individual models and spatially among models with different L values. Specifically, P-waves associated with the fast outer formation progressively overtake those in the slow inner formation, arriving earlier at borehole receivers. This process is primarily controlled by the formation interface position: closer interfaces cause earlier wave overlap, whereas increasing interface distance delays the overtaking process. If the interface is sufficiently distant, overtaking is completely suppressed. During this transition, constructive interference between the two waves leads to amplitude superposition, resulting in a significant increase in the total P-wave energy. Simultaneously, phase differences between the two waves cause destructive interference, leading to noticeable fluctuations in the dominant frequency. Moreover, when the near-borehole interface has a small dip angle, mode conversion of the first-arrival still occurs. However, the dip angle can systematically bias the estimated P-wave velocity of the fast formation. A negative dip tends to advance the fast P-wave arrival and yield an overestimated velocity, whereas a positive dip delays the fast P-wave arrival and yields an underestimated velocity. Therefore, the interface dip angle should be explicitly considered in the velocity-correction procedure.

5. Formation interface effects on horizontal borehole wave modes under multi-interface conditions

The previous analysis examined the mechanism of formation-interface influence on borehole wave modes based on a two-layer model. Building on this analysis, a three-layer horizontal

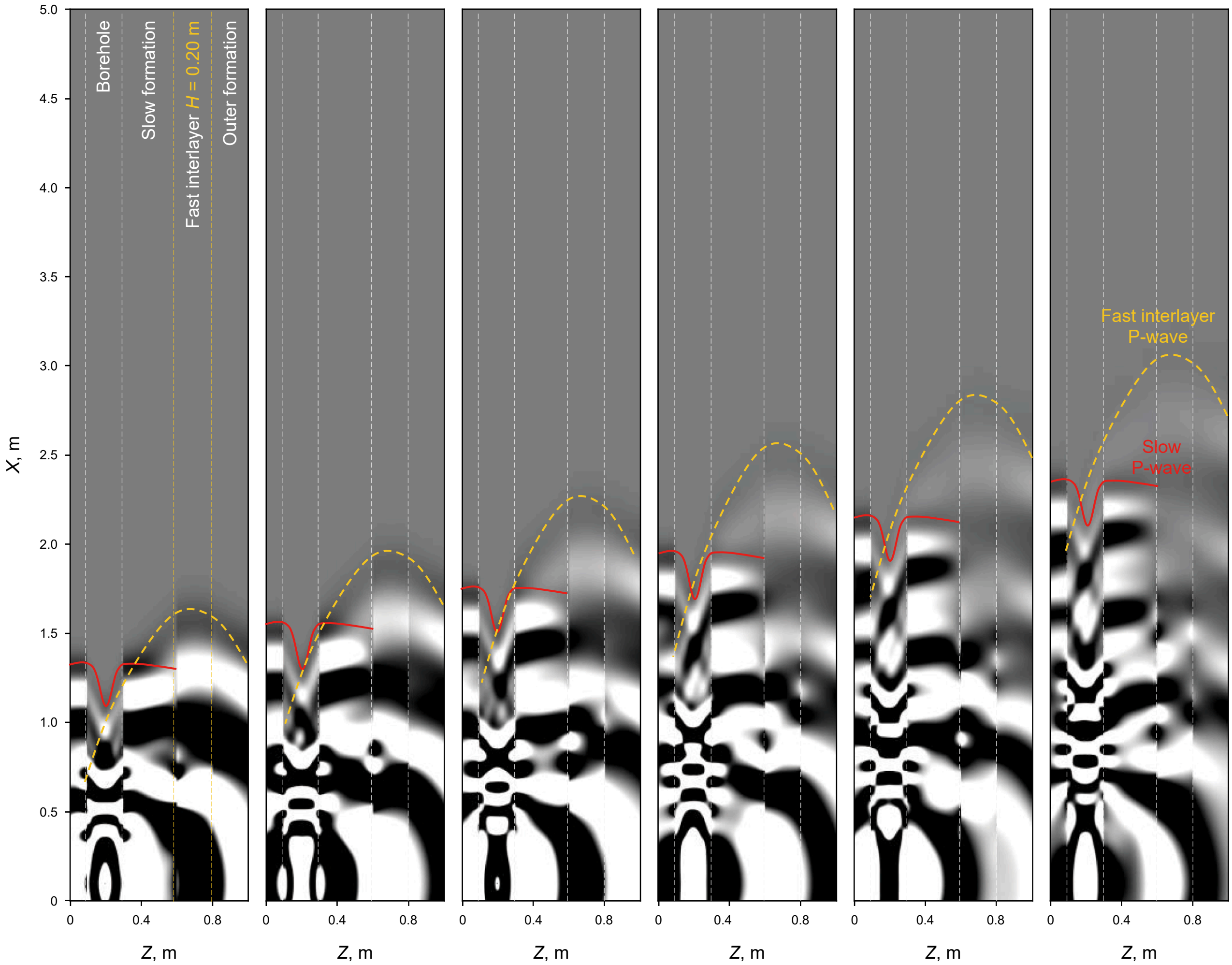

Fig. 23. Wavefield snapshots of the fast-interlayer model at different time steps (t).

well formation model was developed to examine the effects of multi-interface coupling on borehole wave mode responses.

Building on the two-layer model, a three-layer formation model was developed by introducing an interlayer between the fast and slow formations. The interlayer forms Interface 1 with the slow formation, and Interface 2 with the fast formation (see Fig. 19). Its wave velocity is intermediate between those of the fast and slow formations, and its material properties are listed in Table 4. In the simulation, Interface 1 was fixed at L_1= 0.30 m, while the interlayer thickness (H) was varied from 0.15 to 0.40 m with 0.05 m increments, corresponding to L_2 values of 0.45 to 0.70 m. To ensure sufficient detection depth of borehole wave modes, the maximum TR spacing was increased to 3.0 m, and the dominant frequency of the transmitter was set to 10 kHz.

Fig. 20 illustrates wavefield snapshots at various time steps for interlayer thicknesses of H = 0.15 m and 0.40 m.

The results indicate that, for a thin interlayer (as seen in Fig. 20(a)), the borehole first-arrival transitions directly from the slow P-wave (red curve) to the fast P-wave (blue curve) as propagation time increases. The interlayer P-wave (yellow curve) only becomes discernible at larger TR spacings, when the P-wave components are separated, and appears between the slow and fast P-waves. With a thicker interlayer (as seen in Fig. 20(b)), the first-arrival initially transitions from the slow P-wave to the interlayer P-wave before finally transitioning to the fast P-wave.

According to the preceding theoretical analysis, when the interface is sufficiently distant, the P-wave originating from the outer fast formation cannot overtake that from the inner slow formation before it reaches the receiver. In this case, Interface 1 remains fixed, thus keeping constant the overtaking time (t_1) of the interlayer P-wave relative to that of the slow P-wave. As Interface 2 moves farther away, the arrival time of the fast P-wave (t_2) is delayed. The interlayer P-wave becomes the borehole first-arrival once $t_2 > t_1$ (Fig. 21).

The TR–L spectrum of P-wave parameters in Fig. 22 validates the previously described process, where L denotes the distance from Interface 2 to the borehole axis (L_2). Variations in P-wave velocity, dominant frequency, and energy produce three distinct boundaries in the figure, which indicate P-wave mode conversions induced by multiple formation interfaces. These boundaries are distinguished by distinct colors: the purple solid line denotes the conversion from the interlayer P-wave to the fast P-wave; the red dashed line denotes the transition from the fast P-wave to the slow P-wave; and the black long-dashed line denotes the transition from the interlayer P-wave to the slow P-wave. By these boundaries, the TR–L spectrum is divided into several regions.

The triangular region in the upper left represents the fast formation, characterized by a P-wave velocity greater than 6000 m/s, a steady dominant frequency of approximately 13.5 kHz, and relatively low energy. The triangular region in the right center

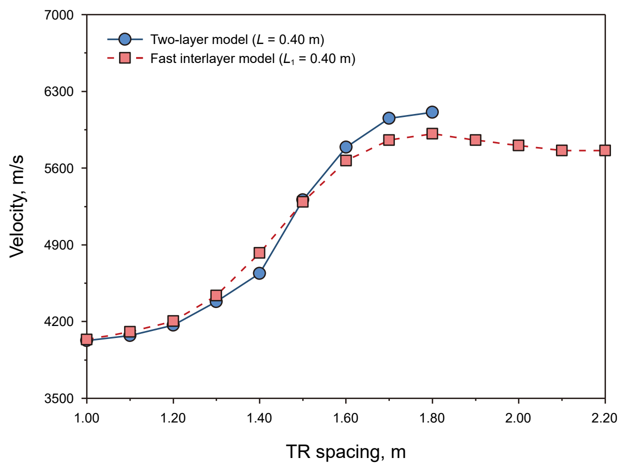

Fig. 24. Comparison of P-wave velocity variations with TR spacing between the two-layer and fast-interlayer models.

represents the interlayer, with a P-wave velocity of approximately 5100 m/s. Resulting from mode conversions with the fast and slow formation P-waves, its dominant frequency is oscillatory and relatively low, while its energy fluctuates due to interference from overlapping waveforms. The bottom rectangular region (TR < 1.6 m) represents the slow formation, characterized by a low P-wave velocity of approximately 4200–4600 m/s, a stable dominant frequency near 15 kHz, and locally enhanced energy resulting from constructive interference during mode conversions.

Furthermore, when Interface 1 is fixed, variations in interlayer thickness (H) have no effect on the time of overlap between the slow and interlayer P-waves. Consequently, the TR value corresponding to the black boundary remains constant and exhibits a horizontal trend. The interlayer-fast and fast-slow P-wave conversions exhibit inclined trends as the interlayer thickness increases (i.e., as Interface 2 moves farther from the borehole axis), consistent with the P-wave mode conversion patterns observed in the two-layer model.

A fast-interlayer model was constructed by interchanging the material properties between the fast formation and the interlayer. Wavefield snapshots for this model are shown in Fig. 23.

The figure illustrates that as propagation time increases, the fast-interlayer P-wave overtakes the slow P-wave and emerges as the first-arrival. In contrast, the slower outer-formation P-wave does not participate in this process. The relationship between P-wave velocity and TR in Fig. 24 further validates this behavior: as TR increases, the first-arrival velocity increases from approximately 4000 m/s (slow-formation P-wave) to about 6000 m/s (fast-interlayer P-wave) before stabilizing, exhibiting a pattern consistent with that of the two-layer model.

In summary, the response characteristics of P-waves under the coupling effects of multiple interfaces were revealed through wavefield and TR–L spectrum analyses of multilayer formation models. These results further validate the mechanism by which formation interfaces influence borehole wave modes.

6. Conclusions

This study conducted numerical simulations to investigate the influence of adjacent formation interfaces on acoustic wave modes in horizontal wells. The effects of the interfaces on the velocity, energy, and dominant frequency of borehole wave modes were systematically analyzed. Wavefield snapshots were analyzed to elucidate the underlying mechanisms governing interface-induced variations in acoustic wave propagation. The main findings are summarized as follows:

The effect of the adjacent formation interface on borehole wave modes is primarily attributed to the mode conversion occurring in the first-arrivals, which predominantly influences P-wave characteristics—including velocity, energy, and dominant frequency—while exerting a relatively minor impact on S-waves.

The mode conversion of the first-arrival is primarily governed by the dynamic interaction between fast and slow P-waves from different formations, in which the fast P-wave overtakes the slow P-wave. This process is largely governed by the formation interface distance and interface dip angle, with the overlap time of the two waves positively correlated with it.

Variations in borehole first-arrival velocity arise from the conversion between the fast and slow P-waves across the formation interface. During mode conversion, constructive interference locally increases P-wave energy, and the dominant frequency oscillates. The effects of interface distance and TR spacing on wave mode velocity, energy, and dominant frequency were summarized.

The TR spacing at which the two waves interfere shows a linear relationship with both the interface distance and dip angle. However, the dip angle can bias the estimated P-wave velocity of the fast formation: a negative dip angle leads to an overestimation of the velocity, whereas a positive dip angle results in an underestimation. This bias primarily stems from the variations in wave propagation path lengths induced by the interface inclination. Therefore, it should be included in the velocity-correction procedure.

Borehole wave mode responses under multi-interface coupling conditions can be regarded as the superposition of first-arrival mode conversions between adjacent formations. The behavior of wave mode parameters in this process is consistent with the theoretical predictions.

In future work, physical experiments on formation models with near-borehole interfaces will be conducted, and quantitative relationships may be established by incorporating the interface position, acoustic impedance contrast between formations, and P-wave characteristic parameters. Such relationships would enable more accurate extraction and correction of wave mode slowness and amplitude attenuation for horizontal well acoustic logging.

CRediT authorship contribution statement

Zhi-Yang Lei: Writing – original draft, Investigation, Data curation. **Yi Xin:** Software, Project administration, Formal analysis. **Dong Wu:** Validation, Methodology, Formal analysis. **Ming Cai:** Supervision, Project administration, Funding acquisition, Conceptualization. **Xin-Jian Zhao:** Validation, Software. **Cheng-Guang Zhang:** Supervision, Methodology, Conceptualization. **Yuan-Jun Zhang:** Writing – review & editing, Formal analysis. **Shi-Hong Luo:** Writing – review & editing, Investigation.

Declaration of competing interest

The authors declare that they have no known competing financial interests or personal relationships that could have appeared to influence the work reported in this paper.

Acknowledgments

This work was supported by the National Natural Science Foundation of China (42474177, 42104126) and CNPC Innovation Foundation (2022DQ02-0301).

References

Alford, R.M., Kelly, K.R., Boore, D.M., 1974. Accuracy of finite-difference modeling of the acoustic wave equation. Geophysics 39 (6), 834–842. https://doi.org/10.1190/1.1440470.

Cai, M., Wu, H., Liu, P., et al., 2022a. Intelligent calculation method of relative sonic attenuation and its application to fracture evaluation in tight sandstone reservoir. J. Petrol. Sci. Eng. 218, 110968. https://doi.org/10.1016/j.petrol.2022.110968.

Cai, M., Wu, H., Xin, Y., et al., 2022b. Experimental study on shear wave transmission in fractured media. Sensors 22 (11), 4047. https://doi.org/10.3390/s22114047.

Cai, M., Zhang, C., Han, C., et al., 2020. Experimental research of effect of microfracture on shear wave attenuation and its application on fracture evaluation in tight sand formation. J. China Univ. Pet (Ed. Nat. Sci.) 44 (1), 45–52. https://doi.org/10.3969/j.issn.1673-5005.2020.01.005 (in Chinese).

Che, X., Qiao, W., Wang, R., 2009. MPAL cross-dipole array acoustic logging data processing. In: 2009 2nd International Congress on Image and Signal Processing, pp. 1–4. https://doi.org/10.1109/CISP.2009.5304322.

Chen, H., Wang, X., Zhao, H., 2006. A rotated staggered grid finite-difference with the absorbing boundary condition of a perfectly matched layer. Chin. Sci. Bull. 51, 2304–2314. https://doi.org/10.1007/s11434-006-2127-8.

Cong, J., Qiao, W., 2008. Simulated response of acoustic log in horizontal borehole placing on interface of two formations. Well Logging Technol. 32 (1), 29–32. https://doi.org/10.16489/j.issn.1004-1338.2008.01.022 (in Chinese).

Feng, F., 2023. Research on the progress of horizontal well drilling technology. West. Explor. Eng. 35 (7), 99–101. https://doi.org/10.3969/j.issn.1004-5716.2023.07.032 (in Chinese).

Gao, Z., Wu, D., Wu, H., et al., 2024. Numerical simulation study on the influence of fracture on borehole wave modes: insights from fracture width, filling condition, and acoustic frequency. Sensors 24 (12), 3955. https://doi.org/10.3390/s24123955.

Graves, R.W., 1996. Simulating seismic wave propagation in 3D elastic media using staggered-grid finite differences. Bull. Seismol. Soc. Am. 86 (4), 1091–1106. https://doi.org/10.1785/BSSA0860041091.

Hei, C., Hu, W., Zou, X., et al., 2024. Numerical simulation of acoustic field ahead of drill bit in formation generated by multipole source during logging while drilling. IEEE Geosci. Remote Sens. Lett. 21, 7506705. https://doi.org/10.1109/LGRS.2024.3433456.

Huang, S., Torres-Verdín, C., 2017. Fast-forward modeling of compressional arrival slowness logs in high-angle and horizontal wells. Geophysics 82 (2), D107–D122. https://doi.org/10.1190/geo2016-0317.1.

Ji, Y., He, X., Chen, H., et al., 2021. The effects of tool eccentricity on individual P and S head waves in monopole acoustic LWD. J. Geophys. Eng. 18 (1), 74–84. https://doi.org/10.1093/jge/gxaa069.

Li, J., Wan, J., Wang, T., et al., 2022. Leakage simulation and acoustic characteristics based on acoustic logging by ultrasonic detection. Adv. Geo-Energy Res. 6 (3), 181–191. https://doi.org/10.46690/ager.2022.03.02.

Lin, W., Wang, X., Zhang, H., 2006. Acoustic wave propagation in a borehole penetrating an inclined layered formation. Chin. J. Geophys. 49 (1), 234–246. https://doi.org/10.1002/cjg2.831 (in Chinese).

Liu, G., 2021. Challenges and countermeasures of log evaluation in unconventional petroleum exploration and development. Petrol. Explor. Dev. 48 (5), 1033–1047. https://doi.org/10.1016/S1876-3804(21)60089-7.

Liu, H., Wang, B., Tao, G., et al., 2017. Study on the simulation of acoustic logging measurements in horizontal and deviated wells. Appl. Geophys. 14, 337–350. https://doi.org/10.1007/s11770-017-0637-6.

Liu, P., Fan, H., Zhang, M., et al., 2025. Response characteristics of shear waves scattered by fractures with borehole observation system. Pet. Sci. 22 (5), 1912–1928. https://doi.org/10.1016/j.petsci.2025.03.004.

Liu, P., Qiao, W., Che, X., et al., 2016. Numerical simulation of azimuthal acoustic logging in a borehole penetrating a rock formation boundary. Geophysics 81 (3), D283–D291. https://doi.org/10.1190/geo2015-0265.1.

Ma, C., Gao, Y., Lu, C., 2019. Numerical modeling of elastic wave in frequency-domain by using staggered grid fourth-order finite-difference scheme. Adv. Geo-Energy Res. 3 (4), 410–423. https://doi.org/10.26804/ager.2019.04.08.

Ma, K., Wang, B., Jiang, K., et al., 2025. Numerical simulation method and application of high-performance acoustic remote detection imaging in fractured reservoirs. IEEE Trans. Geosci. Rem. Sens. 63, 1–12. https://doi.org/10.1109/TGRS.2025.3581337.

Pan, Y., He, X., Chen, H., et al., 2022. Acoustic field simulations of logging while drilling by cylindrical finite difference with variable grids. Appl. Geophys. 19, 11–28. https://doi.org/10.1007/s11770-022-0922-x.

Pan, Y., He, X., Wang, X., 2023. 3D viscoelastic finite-difference analysis of the monopole acoustic logs in cylindrical coordinates. J. Theor. Comp. Acout. 31 (1), 2250006. https://doi.org/10.1142/S2591728522500062.

Passey, Q.R., Yin, H., Rendeiro, C., et al., 2005. Overview of high-angle and horizontal well formation evaluation: issues, learnings, and future directions. In: SPWLA Annual Logging Symposium, SPWLA-2005-A.

Qiao, W., Ju, X., Che, X., et al., 2011. Progress in acoustic well logging technology. Well Logging Technol. 35 (1), 14–19. https://doi.org/10.16489/j.issn.1004-1338.2011.01.003 (in Chinese).

Randall, C.J., Scheibner, D.J., Wu, P.T., 1991. Multipole borehole acoustic waveforms: Synthetic logs with beds and borehole washouts. Geophysics 56 (11), 1757–1769. https://doi.org/10.1190/1.1442988.

Rostami, A., Kordavani, A., Parchekhari, S., et al., 2022. New insights into permeability determination by coupling Stoneley wave propagation and conventional petrophysical logs in carbonate oil reservoirs. Sci. Rep. 12, 11618. https://doi.org/10.1038/s41598-022-15869-1.

Stephen, R.A., Cardo-Casas, F., Cheng, C.H., 1985. Finite-difference synthetic acoustic logs. Geophysics 50 (10), 1588–1609. https://doi.org/10.1190/1.1441849.

Su, L., Cai, M., Zheng, Z., et al., 2022. Numerical simulation of the effects of borehole enlargement on sonic logging response of horizontal wells. Geophys. Geochem. Explor. 46 (2), 467–473. https://doi.org/10.11720/wtyht.2022.2447 (in Chinese).

Su, Y., 2018. Introduction to the theory and technology on downhole control engineering and its research progress. Petrol. Explor. Dev. 45 (4), 754–763. https://doi.org/10.1016/S1876-3804(18)30078-8.

Tang, X.M., Cheng, A.C.H., 2004. Quantitative Borehole Acoustic Methods. Elsevier, Amsterdam, Boston.

Wang, H., Toksöz, M.N., Fehler, M.C., 2020. Wave propagation in an open borehole. In: Wang, H., Toksöz, M.N., Fehler, M.C. (Eds.), Borehole Acoustic Logging – Theory and Methods. Springer International Publishing, Cham, pp. 17–58. https://doi.org/10.1007/978-3-030-51423-5_2.

Wang, R., Herrera, W., Torres-Verdín, C., 2017. Simulation and interpretation of sonic waveforms in high-angle and horizontal wells. Geophysics 82 (4), D251–D263. https://doi.org/10.1190/geo2016-0402.1.

Wang, R., Qiao, W., 2014. Numerical study of cross-dipole acoustic logging in fluid-filled borehole with an eccentric drill collar. Chin. J. Geophys. 57 (6), 2013–2023. https://doi.org/10.6038/cjg20140631 (in Chinese).

Wang, X., Zhang, H., Wang, D., 2003. Modelling seismic wave propagation in heterogeneous poroelastic media using a high-order staggered finite-difference method. Chin. J. Geophys. 46 (6), 1206–1217. https://doi.org/10.1002/cjg2.441 (in Chinese).

Wei, Z., Chen, X., 2015. Wave-field analysis and velocity correction chart making of the tilted formation with a fluid-filled borehole. Acta Acustica 40 (3), 437–445. https://doi.org/10.15949/j.cnki.0371-0025.2015.03.011 (in Chinese).

Wood, D.A., 2024. Expanding role of borehole image logs in reservoir fracture and heterogeneity characterization: A review. Adv. Geo-Energy Res. 12 (3), 194–204. https://doi.org/10.46690/ager.2024.06.04.

Xu, F., Wang, Z., 2020. Numeric simulation of acoustic-logging of cave formations. Energies 13 (15). https://doi.org/10.3390/en13153908.

Yang, B., Zhang, C., Cai, M., et al., 2019. Research on evaluation method of fracture permeability based on Stoneley wave energy attenuation. Prog. Geophys. 34 (3), 1127–1131. https://doi.org/10.6038/pg2019CC0121 (in Chinese).

Yang, S., Qiao, W., Che, X., 2018. A hybrid parallel finite difference algorithm for 3D elastic wave equation based on MPI and OpenMP. J. Appl. Acoust. 37 (1), 75–82. https://doi.org/10.11684/j.issn.1000-310X.2018.01.011 (in Chinese).

Zhang, Y., Wu, D., Liao, M., et al., 2024. Impact of tool eccentricity on acoustic logging response in horizontal wells: insights from physical simulation experiments. Geofluids (1), 8071443. https://doi.org/10.1155/2024/8071443.

Zhao, H., Wang, X., Wang, D., et al., 2007. Applications of the boundary absorption using a perfectly matched layer for elastic wave simulation in poroelastic media. Chin. J. Geophys. 50 (2), 513–525. https://doi.org/10.1002/cjg2.1061 (in Chinese).

Zhou, C., Wang, C., 2006. Technology review on the log interpretation of horizontal well. Prog. Geophys. 21 (1), 152–160. https://doi.org/10.3969/j.issn.1004-2903.2006.01.022 (in Chinese).